



The relative abundances of resolved $^{12}\text{CH}_2\text{D}_2$ and $^{13}\text{CH}_3\text{D}$ and mechanisms controlling isotopic bond ordering in abiotic and biotic methane gases

E.D. Young^{a,*}, I.E. Kohl^a, B. Sherwood Lollar^b, G. Etiope^{c,d}, D. Rumble III^e, S. Li (李姝宁)^a, M.A. Haghnegahdar^a, E.A. Schauble^a, K.A. McCain^a, D.I. Foustoukos^e, C. Sutcliffe^b, O. Warr^b, C.J. Ballentine^f, T.C. Onstott^g, H. Hosgormez^h, A. Neubeckⁱ, J.M. Marques^j, I. Pérez-Rodríguez^k, A.R. Rowe^k, D.E. LaRowe^k, C. Magnabosco^l, L.Y. Yeung^m, J.L. Ash^a, L.T. Bryndziaⁿ

^a University of California Los Angeles, United States

^b University of Toronto, Canada

^c Istituto Nazionale di Geofisica e Vulcanologia, Sezione Roma 2, Italy

^d Faculty of Environmental Science and Engineering, Babes-Bolyai University, Cluj-Napoca, Romania

^e Carnegie Institution of Washington, United States

^f University of Oxford, United Kingdom

^g Princeton University, United States

^h Istanbul University, Republic of Turkey

ⁱ Stockholm University, Sweden

^j Universidade de Lisboa, Portugal

^k University of Southern California, United States

^l Simons Foundation, United States

^m Rice University, United States

ⁿ Shell International Exploration and Production Inc., United States

Received 11 August 2016; accepted in revised form 31 December 2016; Available online 11 January 2017

Abstract

We report measurements of resolved $^{12}\text{CH}_2\text{D}_2$ and $^{13}\text{CH}_3\text{D}$ at natural abundances in a variety of methane gases produced naturally and in the laboratory. The ability to resolve $^{12}\text{CH}_2\text{D}_2$ from $^{13}\text{CH}_3\text{D}$ provides unprecedented insights into the origin and evolution of CH_4 . The results identify conditions under which either isotopic bond order disequilibrium or equilibrium are expected. Where equilibrium obtains, concordant $\Delta^{12}\text{CH}_2\text{D}_2$ and $\Delta^{13}\text{CH}_3\text{D}$ temperatures can be used reliably for thermometry. We find that concordant temperatures do not always match previous hypotheses based on indirect estimates of temperature of formation nor temperatures derived from CH_4/H_2 D/H exchange, underscoring the importance of reliable thermometry based on the CH_4 molecules themselves. Where $\Delta^{12}\text{CH}_2\text{D}_2$ and $\Delta^{13}\text{CH}_3\text{D}$ values are inconsistent with thermodynamic equilibrium, temperatures of formation derived from these species are spurious. In such situations, while formation temperatures are unavailable, disequilibrium isotopologue ratios nonetheless provide novel information about the formation mechanism of the gas and the presence or absence of multiple sources or sinks. In particular, disequilibrium isotopologue ratios may provide the means for differentiating between methane produced by abiotic synthesis vs. biological processes. Deficits in $^{12}\text{CH}_2\text{D}_2$ compared with equilibrium values in CH_4 gas made by surface-catalyzed abiotic reactions are so large

* Corresponding author.

E-mail address: eyoung@epss.ucla.edu (E.D. Young).

as to point towards a quantum tunneling origin. Tunneling also accounts for the more moderate depletions in $^{13}\text{CH}_3\text{D}$ that accompany the low $^{12}\text{CH}_2\text{D}_2$ abundances produced by abiotic reactions. The tunneling signature may prove to be an important tracer of abiotic methane formation, especially where it is preserved by dissolution of gas in cool hydrothermal systems (e.g., Mars). Isotopologue signatures of abiotic methane production can be erased by infiltration of microbial communities, and $\Delta^{12}\text{CH}_2\text{D}_2$ values are a key tracer of microbial recycling.

© 2017 Elsevier Ltd. All rights reserved.

Keywords: Methane isotopes; Isotope clumping

1. INTRODUCTION

Measurements of multiply-substituted $^{13}\text{CH}_3\text{D}$ species in CH_4 gas have been used recently to estimate temperatures of formation of natural gases, identify gases of microbial origin that exhibit departures from isotopic bond-order equilibrium, and to elucidate mixing between thermogenic and biogenic methane (Ono et al., 2014; Stolper et al., 2014a,b, 2015; Wang et al., 2015). Beginning in 2008, we embarked on a project to develop and employ a prototype mass spectrometer that is capable of resolving the two mass-18 isotopologues of methane, $^{12}\text{CH}_2\text{D}_2$ and $^{13}\text{CH}_3\text{D}$, for high-precision isotope ratio analysis (Young et al., 2016). Here we report measurements of resolved $^{12}\text{CH}_2\text{D}_2$ and $^{13}\text{CH}_3\text{D}$ at natural abundances made using this instrument. Samples include a variety of methane gases produced naturally and in the laboratory. The use of two multiply-substituted isotopic species provides insights into the provenance of methane gases, the physical chemical pathways of methane formation, and subsequent processing.

Reasons for studying the isotopic compositions of methane molecules are far ranging. The origins of natural gases, a major source of energy for the near future, serves as an important example. Another is the highly uncertain global atmospheric budget of methane, a key greenhouse gas. Yet another is the discovery of methane in the atmosphere of Mars as well as methane emanations from martian meteorites (Blamey et al., 2015; Webster et al., 2015). Indeed, methane and other alkanes are prevalent in outer solar system bodies (e.g., Brown et al., 2008), and there is the need to identify formation pathways of methane gas throughout the solar system. In extra-terrestrial applications, isotopic bond ordering can be particularly useful where our understanding of the bulk isotope ratios of various relevant reservoirs is poor to nonexistent.

One of the most pressing issues concerning the provenance of CH_4 gases is the need for reliable signatures of abiotic vs. biotic sources (Sherwood Lollar et al., 2006; Etiope and Sherwood Lollar, 2013). The major sources of methane in commercial natural gas fields are biotic, coming either from thermal cracking of sedimentary organic material (primary thermogenic) or oil (secondary thermogenic), or from microbial methanogenesis (microbialgenic or “biogenic”) (e.g., Schoell, 1988). Abiotic methane is produced in abundance in some geological settings such as marine hydrothermal vents (Kelley et al., 2005; Proskurowski et al., 2008), in continental ultramafic terranes exposed to fluids leading to serpentinization (Horita and Berndt, 1999; Etiope and

Sherwood Lollar, 2013; Schrenk et al., 2013) and in terrestrial Precambrian crust related to H_2 production from both serpentinization and radiolysis of water (Sherwood Lollar et al., 2002, 2014). While comprising globally significant sources of methane, these abiotic sources are generally regarded as being of little commercial significance due to the ephemeral and unpredictable nature of their reservoirs deep in fractured crystalline rocks (Sherwood Lollar et al., 2002; Glasby, 2006). Nonetheless, the origin of gas in the world’s second largest gas field, Urengoy in Western Siberia, has been attributed variously to bacterial methane generation, thermal breakdown of deeply buried mature organic matter, and abiotic thermocatalytic reduction of CO_2 (Cramer et al., 1998 and references therein).

The typical isotopic tracers of methane provenance are $^{13}\text{C}/^{12}\text{C}$ (reported as $\delta^{13}\text{C}^1$ relative to VPDB) and D/H (reported as δD relative to VSMOW). While isotope ratios of carbon and hydrogen have proved useful for tracing the origins of natural methane (Schoell, 1988; Etiope and Sherwood Lollar, 2013), these ratios by themselves can be ambiguous; there is overlap between some empirically derived ranges defined by these isotope ratios for different sources of methane. For example, the carbon isotope ratios associated with thermogenic methane formation and microbial activity, partially overlap with those for abiotic methane formation (Horita and Berndt, 1999; Tang et al., 2000; Cramer, 2004).

The ambiguity is exacerbated by the fact that in many geological settings methane sources are likely to be mixed (Etiope and Sherwood Lollar, 2013). A mixture of thermogenic and microbialgenic gas is difficult if not impossible to identify using just bulk $\delta^{13}\text{C}$ and δD , but should be identifiable using isotopic bond ordering (e.g., Young et al., 2011, 2016; Stolper et al., 2015). Other geochemical signatures of methane formation pathways can help disambiguate the conclusions based on bulk isotope ratios alone. For example, a decrease in $\delta^{13}\text{C}$ with increasing carbon number for gaseous n-alkanes (C1–C4) can be a line of evidence for abiotic formation, while a strongly positive relationship between $\delta^{13}\text{C}$ and carbon number reflects a thermogenic origin (Sherwood Lollar et al., 2002; McCollom and Seewald, 2007). However, the $^{13}\text{C}/^{12}\text{C}$ composition of hydrocarbons experimentally formed during Fischer–Tropsch-Type (FTT) synthesis under hydrothermal

¹ Throughout this paper we make use of the convention dating back to McKinney et al. (1950) that delta symbols refer to per mil deviations of an isotope ratio from a standard. All small and capital delta symbols in this work have units of per mil.

conditions (McCollom and Seewald, 2006; Fu et al., 2007) and measured in the alkaline vent fluids of Lost City (Proskurowski et al., 2008) appear to deviate from the “abiotic” trends referred to above. This suggests that the magnitude of fractionations and isotopic trends among light alkanes are likely affected by mineral-catalyst composition and the kinetic rates of FTT reactions (Sherwood Lollar et al., 2008). By characterizing the bond ordering of ^{13}C and D in CH_4 , the role of methane formation mechanism on the C–H bond can be assessed in the absence of subsequent polymerization reactions. It is evident, therefore, that an ideal and robust tracer for methane formation mechanisms would be one based on the methane molecule itself.

The initial motivation for the development of methane isotopologue tracers was the utility of $^{13}\text{CH}_3\text{D}/^{12}\text{CH}_4$ ratios as formation temperature indicators. Intermolecular isotope exchange thermometers like D/H exchange between CH_4 and H_2 gas rely on the assumption of exchange equilibrium. An intra-species thermometer would be more robust. Methane sources that can be distinguished on the basis of temperature include microbial production in sedimentary source rocks with an upper temperature limit of ~ 70 to 90 °C and higher-temperature thermogenic methane production that often occurs at >140 °C, or abiotic methane produced in high-temperature hydrothermal systems at >300 °C. However, temperature alone will not be entirely diagnostic. Thermogenic methane can be produced at temperatures as low as 60 – 70 °C (diagenesis or low- T catagenesis), overlapping the range for microbial methanogenesis. Serpentinization, a source of hydrogen to produce methane, occurs at temperatures at least as low as 50 °C (Schrenk et al., 2013 and references therein), and so abiotic methane production also overlaps with microbial methanogenesis in temperature (Etiope and Sherwood Lollar, 2013 and references therein). Overlap occurs at high temperatures between thermogenic gas from biotic sources and abiogenic processes like high-temperature oxidation–reduction in the deep crust or mantle (e.g., higher- T serpentinization) and catalyzed abiotic hydrocarbon production by FTT reactions (Horita and Berndt, 1999; Foustoukos and Seyfried, 2004; Etiope and Ionescu, 2015). In addition, it is difficult to verify that a temperature derived from a measurement of $^{13}\text{CH}_3\text{D}/\text{CH}_4$ alone is valid; assessment of the degree of internal (intra-species) thermodynamic equilibrium is necessary to verify that a temperature obtained by isotopic bond ordering is valid.

Rather than relying on temperature estimates alone, the long-term goal should be to characterize the effects of various reactions and transport mechanisms on the distributions of rare isotopologues. The goal of this study is to investigate the advantages of using the relative concentrations of $^{12}\text{CH}_2\text{D}_2$ and $^{13}\text{CH}_3\text{D}$ to elucidate the origin of methane gas from a wide variety of geochemical settings. In particular, we set out to characterize methane produced abiotically, generally by surface catalysis, and to compare those gases to those produced by microbial methanogenesis and to those originating from thermogenesis. We do this by analyzing samples produced in the laboratory and samples representing various natural sources of methane gas.

2. FUNDAMENTALS OF $\Delta^{12}\text{CH}_2\text{D}_2$ VS. $\Delta^{13}\text{CH}_3\text{D}$ SPACE

2.1. Temperature

The concept of isotope bond ordering, or “clumping” as it has become known in the geosciences, is understood relative to the null condition of the purely stochastic distribution of isotopic species (isotopologues) of a molecule. In the case of methane one is concerned with the fraction of carbon that is the heavy isotope, ^{13}C :

$$X(^{13}\text{C}) = \frac{^{13}\text{C}}{^{13}\text{C} + ^{12}\text{C}} \quad (1)$$

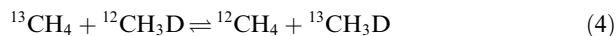
and the fraction of the hydrogen isotopes that is deuterium, D :

$$X(\text{D}) = \frac{\text{D}}{\text{D} + \text{H}} \quad (2)$$

The random distribution of isotopologues is then derived by treating these fractional abundances as probabilities such that, for example

$$\begin{aligned} X(^{12}\text{CH}_4) &= X(^{12}\text{C}) (X(\text{H}))^4 \\ X(^{13}\text{CH}_4) &= X(^{13}\text{C}) (X(\text{H}))^4 \\ X(^{12}\text{CH}_3\text{D}) &= 4X(^{12}\text{C}) (X(\text{H}))^3 X(\text{D}) \\ &\vdots \end{aligned} \quad (3)$$

where multiplicity from isotopomer (isotopic isomer) abundances are accounted for by exponents in Eq. (3). Exchange of isotopes between isotopologues occurs by reactions such as



The equilibrium constant for this reaction is

$$K_{\text{Eq},^{13}\text{CD}} = \frac{[^{13}\text{CH}_3\text{D}][^{12}\text{CH}_4]}{[^{13}\text{CH}_4][^{12}\text{CH}_3\text{D}]} \quad (5)$$

where the square brackets denote concentrations that can be equated with the fractional abundances like those in Eq. (3). At high temperatures (≥ 1000 K) the distributions of isotopologues is effectively random (stochastic) and substitution of the fractional abundances in Eq. (3) into the equilibrium constant in Eq. (5) yields

$$\begin{aligned} K_{\text{Eq},^{13}\text{CD},\text{stoch}} &= \frac{[^{13}\text{CH}_3\text{D}][^{12}\text{CH}_4]}{[^{13}\text{CH}_4][^{12}\text{CH}_3\text{D}]} \\ &= \frac{4X(^{13}\text{C})(X(\text{H}))^3 X(\text{D}) X(^{12}\text{C}) (X(\text{H}))^4}{4X(^{12}\text{C})(X(\text{H}))^3 X(\text{D}) X(^{13}\text{C}) (X(\text{H}))^4} = 1. \end{aligned} \quad (6)$$

An equilibrium constant of unity in this case corresponds to a purely random distribution of isotopes among the molecules. At lower temperatures the stabilizing effects of two heavy isotopes bonded together begins to take hold and the equilibrium constant in Eq. (5) gets progressively larger as T goes down. This enhancement in rare multiply-substituted isotopologues, or clumping, is expressed in delta notation as

$$\Delta^{13}\text{CH}_3\text{D} = 10^3 \left(\frac{X^{13}\text{CH}_3\text{D}}{X^{13}\text{CH}_3\text{D, Stochastic}} - 1 \right). \quad (7)$$

Similarly, internal isotope exchange leading to doubly-deuterated methane can be described by the reaction



with the equilibrium constant

$$K_{\text{Eq,CH}_2\text{D}_2} = \frac{[^{12}\text{CH}_2\text{D}_2][^{12}\text{CH}_4]}{[^{12}\text{CH}_3\text{D}]^2}. \quad (9)$$

The stochastic value for the equilibrium constant for reaction (8) is

$$\begin{aligned} K_{\text{Eq,CH}_2\text{D}_2, \text{stoch}} &= \frac{[^{12}\text{CH}_2\text{D}_2][^{12}\text{CH}_4]}{[^{12}\text{CH}_3\text{D}]^2} \\ &= \frac{6X(^{12}\text{C})(X(\text{H}))^2(X(\text{D}))^2X(^{12}\text{C})(X(\text{H}))^4}{[4(X(\text{H}))^3X(\text{D})X(^{12}\text{C})]^2} = \frac{6}{16} \end{aligned} \quad (10)$$

such that a stochastic distribution of isotopes leads to an equilibrium constant of 3/8. Per mil departures from this stochastic ratio are quantified using

$$\Delta^{12}\text{CH}_2\text{D}_2 = 10^3 \left(\frac{X^{12}\text{CH}_2\text{D}_2}{X^{12}\text{CH}_2\text{D}_2, \text{Stochastic}} - 1 \right). \quad (11)$$

The two parameters $\Delta^{12}\text{CH}_2\text{D}_2$ and $\Delta^{13}\text{CH}_3\text{D}$ can serve as independent intra-molecular thermometers where thermodynamic equilibrium obtains. The relationships between

temperature and both $\Delta^{12}\text{CH}_2\text{D}_2$ and $\Delta^{13}\text{CH}_3\text{D}$ are calculable (e.g., [Ma et al., 2008](#); [Webb and Miller, 2014](#); [Liu and Liu, 2016](#)) and the loci of thermodynamic equilibrium in a plot of $\Delta^{12}\text{CH}_2\text{D}_2$ vs. $\Delta^{13}\text{CH}_3\text{D}$ serves as a useful reference ([Fig. 1](#)). *Ab initio* calculations by one of us (EAS) for equilibrium constants yield these expressions used to define the equilibrium curve in $\Delta^{12}\text{CH}_2\text{D}_2$ vs. $\Delta^{13}\text{CH}_3\text{D}$ space:

$$\begin{aligned} K_{\text{Eq,}^{13}\text{CD}} &= 1 + 0.0355502/T - 433.038/T^2 + 1270210.0/T^3 \\ &\quad - 5.94804 \times 10^8/T^4 + 1.196630 \times 10^{11}/T^5 - 9.07230 \times 10^{12}/T^6 \end{aligned} \quad (12)$$

$$\begin{aligned} (8/3)K_{\text{Eq,CH}_2\text{D}_2} &= 1 + 0.183798/T - 785.483/T^2 + 1056280.0/T^3 \\ &\quad + 9.37307 \times 10^7/T^4 - 8.919480 \times 10^{10}/T^5 + 9.901730 \times 10^{12}/T^6 \end{aligned} \quad (13)$$

where T is in K. Differences in the theoretical $\Delta^{13}\text{CH}_3\text{D}$ vs. temperature relationships due to different computational methods are less than the current analytical uncertainties in the measurements for methane ([Webb and Miller, 2014](#); [Liu and Liu, 2016](#)) and the same is most likely true for $\Delta^{12}\text{CH}_2\text{D}_2$.

2.2. Departures from equilibrium

Departures from equilibrium as represented by $\Delta^{12}\text{CH}_2\text{D}_2$ and $\Delta^{13}\text{CH}_3\text{D}$ can arise from bond rupture and bond formation limited by kinetics, but can also arise from any process that alters the bulk isotopic composition

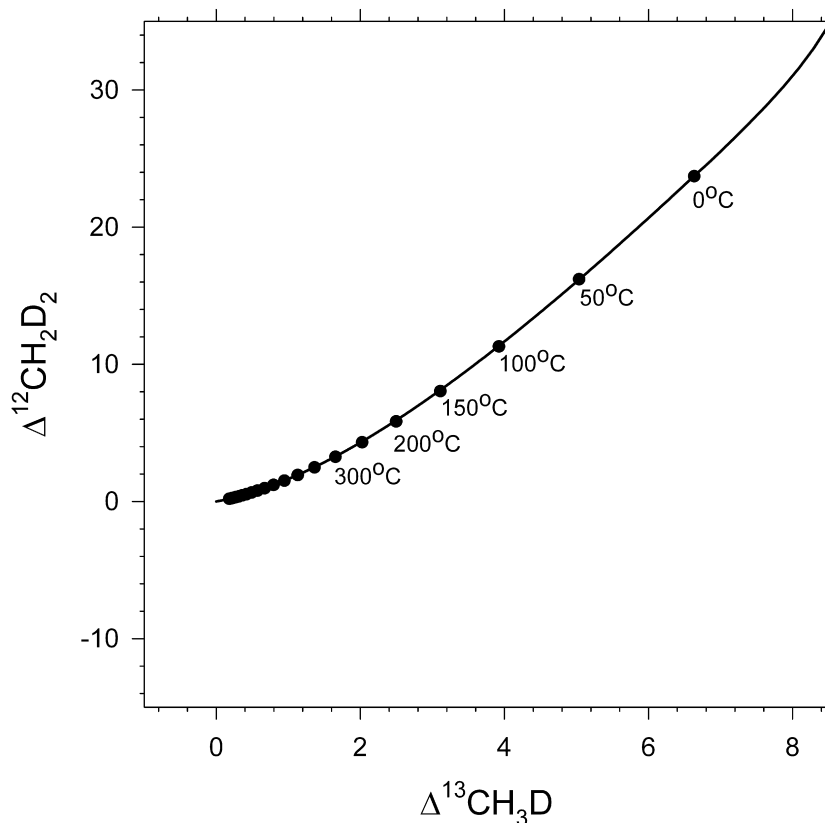


Fig. 1. Thermodynamic equilibrium curve in $\Delta^{12}\text{CH}_2\text{D}_2$ vs. $\Delta^{13}\text{CH}_3\text{D}$ space. Both axes are in per mil.

of the gas. This is because the stochastic ratios comprising the denominators in Eqs. (7) and (11) are calculated from the bulk isotopic compositions, and if these bulk compositions do not represent the values that obtained during bond formation, the shift in reference frame leads to departures from the curve in Fig. 1. One mechanism for departures from the equilibrium curve is therefore mixing of two gases (Eiler and Schauble, 2004). In the case of methane, two CH_4 gases with different bulk $^{13}\text{C}/^{12}\text{C}$ and/or D/H result in clear departures from equilibrium (Young et al., 2016). Fig. 2 shows the effects of mixing as measured in our laboratory (Young et al., 2016). For many naturally-occurring isotope ratios, mixing results in positive excursions from equilibrium. This property of $\Delta^{12}\text{CH}_2\text{D}_2$ vs. $\Delta^{13}\text{CH}_3\text{D}$ space alone is a novel and important new tracer because in many natural methane occurrences mixing of distinct sources (e.g., microbial, thermogenic, abiotic) may have led to inconsistencies in interpretations (Etiope and Sherwood Lollar, 2013).

Kinetics and diffusion are two additional ways to produce deviations from equilibrium $\Delta^{12}\text{CH}_2\text{D}_2$ and $\Delta^{13}\text{CH}_3\text{D}$ values. We have modeled molecular diffusion of CH_4 through an orifice (representing a permeable medium) as a Rayleigh process using Graham's law. Because the slope of molecular diffusion in $\Delta^{12}\text{CH}_2\text{D}_2$ vs. $\Delta^{13}\text{CH}_3\text{D}$ space is nearly unity (because both axes refer to $\sim 18/16$ molecular mass ratios), while the slope of the equilibrium

curve is greater, diffusion results in residues with positive displacements in $\Delta^{12}\text{CH}_2\text{D}_2$ relative to the equilibrium curve (Fig. 3). The greater the diffusive loss, the greater the apparent excess in $^{12}\text{CH}_2\text{D}_2$ in the residual gas relative to equilibrium. Diffused gas behaves similarly but starts out to the right of the equilibrium curve and evolves to the left in Fig. 3. *Ab initio* calculations depicting the kinetics of CH_4 destruction by reaction with the OH radical in the atmosphere (Haghnegahdar et al., 2015) produce a different trajectory in $\Delta^{13}\text{CH}_3\text{D} - \Delta^{12}\text{CH}_2\text{D}_2$ space with negative displacements in the latter (Fig. 3). In both cases, the ability to measure both $\Delta^{13}\text{CH}_3\text{D}$ and $\Delta^{12}\text{CH}_2\text{D}_2$ is crucial for identifying methane affected by these processes.

3. SAMPLES AND METHODS

We report bulk isotopic and isotopologue ratio measurements of methane gases collected from across the globe in a variety of settings, with an emphasis on instances where a significant abiotic component has been reported in previous work. We also present measurements of gases produced in the laboratory by abiotic processes and by microbial methanogenesis. The goal is to use the laboratory experiments as guides for interpreting the results from natural samples, all the while being cognizant of the fact that laboratory conditions cannot mimic the natural conditions perfectly.

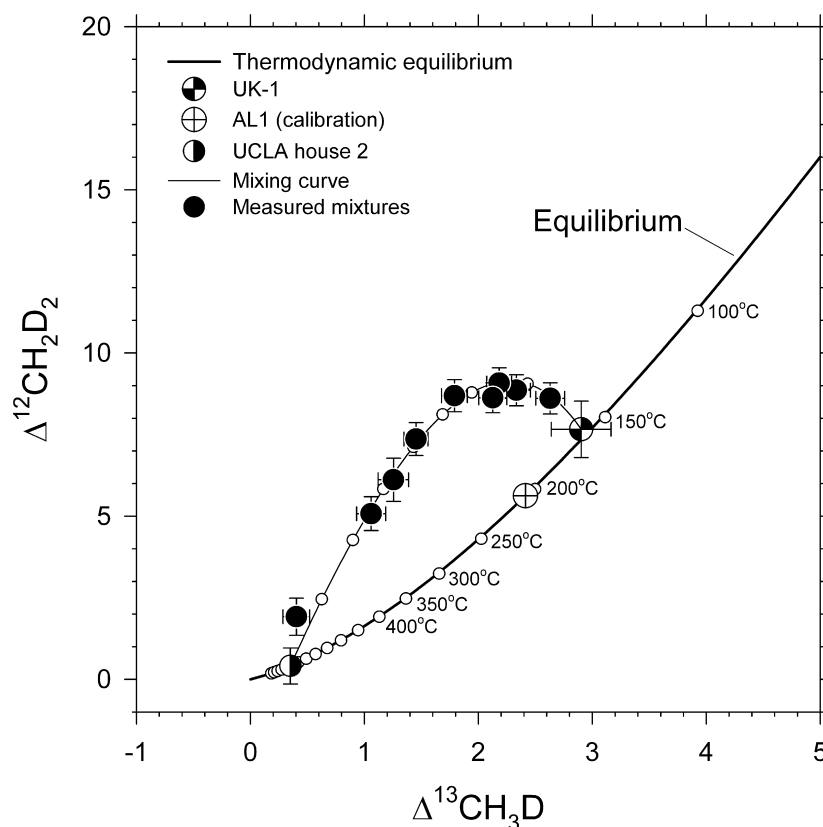


Fig. 2. Measured mixtures (black symbols) of two gases performed in the laboratory at UCLA (Young et al., 2016). The predicted mixing curve is shown with the thin curve and white points marking 10% intervals of mixing. Reproduced from Fig. 12 of Young et al. (2016). Both axes are in per mil.

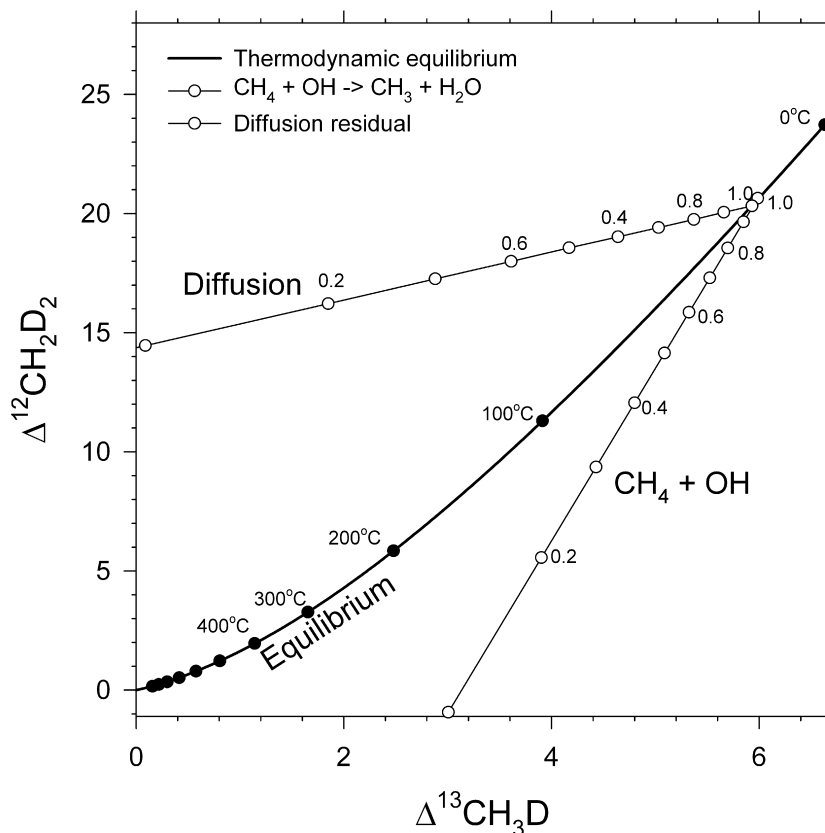


Fig. 3. Comparison of the effects of diffusion and reaction kinetics with thermodynamic equilibrium in $\Delta^{12}\text{CH}_2\text{D}_2$ vs. $\Delta^{13}\text{CH}_3\text{D}$ space. Numbers along trend lines refer to fractions of original gas remaining after Rayleigh fractionation. $\text{CH}_4 + \text{OH}$ kinetics are from Haghnegahdar et al. (2015).

3.1. Natural samples

A pressing problem in determining the provenance of methane gas is distinguishing reliably biotic (microbial production or thermal decomposition of existing organic matter) from abiotic sources. We have therefore sampled sources of putative abiotic CH_4 gas across the globe together with thermogenic gases and gases thought to have a significant microbialgenic component.

3.2. Continent-bound ultramafic igneous complexes

We measured methane gases from three continent-bound ultramafic igneous complexes comprising two obducted ophiolite sequences and a peridotite intrusion. On-shore ultramafic igneous rock terranes such as these have been recognized relatively recently as important sources of abiotic CH_4 (Etiope and Sherwood Lollar, 2013). The largest of these is the Chimaera seep, or “flaming rock” from southwestern Turkey (Fig. 4). Known since antiquity, here methane gas emanates through surface vents from fractures in a 5000 m² outcrop of the Upper Cretaceous Tekirova ophiolite (Etiope et al., 2011). Low-temperature abiotic methane generation is thought to be catalyzed by ruthenium in the host rock (Etiope and Ionescu, 2015). Temperatures of formation have been

estimated to be <100 °C, and perhaps ~50 °C based on the D/H distribution between CH_4 and H_2 and the assumption of inter-species isotopic equilibrium (Etiope et al., 2011). The carbon source for the methane has been dated to be >50,000 years old based on the absence of ¹⁴C (Etiope and Schoell, 2014).

A methane sample from another on-shore igneous complex was collected from a borehole at the Cabeço de Vide mineral water spa, Portugal. Here methane is dissolved in hyperalkaline (pH > 11) waters issuing from natural springs and boreholes drilled in the Alter-do-Chão mafic-ultramafic massif of Ordovician age (Etiope et al., 2013). Serpentinites are distributed to a depth of about 1 km and serpentinization is driven by meteoric water recharge from the surface. At a maximum depth of 1 km and with a temperature gradient of ~30 °C/km, temperatures of formation are thought to be less than 100 °C. Spring waters have a temperature of 20 °C. The exact timing of CH_4 production is uncertain because the role of ongoing reactions vs. storage of older gas is unresolved (Etiope et al., 2013).

We also measured a sample from the Acquasanta Terme hyperalkaline spring waters issuing from serpentinized ophiolites from the north of Italy (Fig. 4) (Boschetti et al., 2013). Here again meteoric waters recharge the system and drive reactions with the ultramafic complex to produce methane at what are believed to be temperatures of

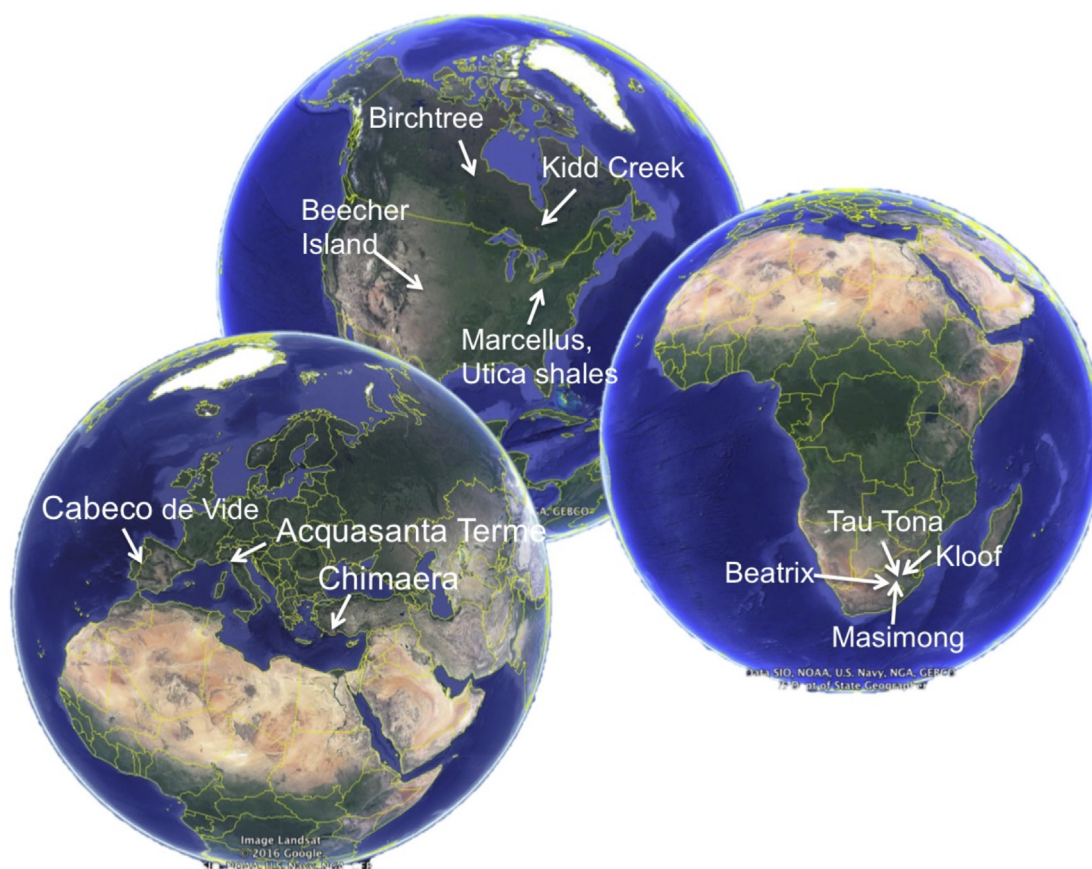


Fig. 4. The locations of methane samples analyzed as part of this survey (Google Earth).

<100 °C. Based on the assumption of D/H equilibrium between H₂O and CH₄, Boschetti et al. estimate a temperature of CH₄ formation of ~60 °C. Methane is free of ¹⁴C, indicating that the carbon source is >50,000 years old (Whiticar and Etiope, 2014).

3.3. Precambrian cratons

Precambrian cratons account for >70% of the continental lithosphere and are now recognized as major contributors to the global budget of H₂ (Sherwood Lollar et al., 2014) that can produce CH₄ from various crustal sources of carbon. The sources of H₂ are thought to be radiolysis of water and/or water–rock reactions at great depth (Sherwood Lollar et al., 2014). Production of CH₄ can occur by abiotic organic synthesis or by microbial methanogenesis where microbial communities are extant in the deep subsurface (Sherwood Lollar et al., 2002, 2006, 2008; Ward et al., 2004; Lin et al., 2006). We analyzed deep mine samples from the Witwatersrand Basin, South Africa and from the Canadian Shield. Sites were selected to represent those with ostensible abiotic CH₄ production, those with a microbial CH₄ source, and also those thought to contain mixtures of the two sources. Sampling methods are similar to those described by Ward et al. (2004).

We analyzed gases from four ultra-deep gold mines from the Witwatersrand Basin, including the Beatrix, Masimong,

Kloof, and Tau Tona mines (Fig. 4). Sampling depths were from ~1 km (Beatrix) to 3.3 km (Kloof). The Witwatersrand lies within the Archean Kaapvaal Craton and is composed of 2900–2500 Ma volcanosedimentary sequences of various lithologies overlying 3450 Ma granite-greenstone and the 3074 Ma volcanosedimentary rocks (Ward et al., 2004). A meteorite impact 2 Gyr before present modified the structure in the central part of the Basin.

Studies from mines throughout the craton have demonstrated the presence of saline aqueous fluids occupying interconnected fractures in the crystalline rocks. The fracture waters from the Witwatersrand Basin are composed of varying proportions of two endmembers consisting of shallower, less saline paleo-meteoric waters and deeper, older, and more saline waters (Onstott et al., 2003; Ward et al., 2004). These paleo-meteoric fracture waters have residence times that range from tens of thousands (Borgonie et al., 2015) to several millions of years (Lippmann et al., 2003). They have negligible dissolved H₂ and are thought to contain CH₄ largely of microbial origin (Ward et al., 2004; Sherwood Lollar et al., 2008). The deeper, more saline fracture waters have high concentrations of dissolved H₂ and are thought to contain abiotic CH₄. They have residence times of tens of millions of years (Lippmann et al., 2003; Lippmann-Pipke et al., 2011).

Waters from the Beatrix, Masimong, and Tau Tona mines are dominated by the paleo-meteoric component.

Beatrix waters have estimated residence times of ~ 3 to 5 million years based on noble gas isotope ratios (Lippmann et al., 2003). Residence times for waters in the Masimong mine can be inferred from noble gas analyses from other mines in the same mining camp and are 1–129 million years (Lippmann et al., 2003). The estimated residence time for the Tau Tona waters is less than 10 million years. In contrast to the other three localities, the Kloof mine waters have isotopic characteristics suggesting the presence of the older, more evolved fluid component. Residence times for the Kloof waters are on the order of 15–20 million years (Lippmann et al., 2003).

Present-day water temperatures in the Witwatersrand mines vary from ~ 30 °C for samples collected at depths of ~ 1 km to ~ 50 °C for the samples collected at ~ 3 km (Kieft et al., 2005; Simkus et al., 2016). Fission track ages from rocks of the Witwatersrand basin indicate that the maximum temperatures of ~ 100 °C existed within the meteoric water flow system $\leq \sim 65$ Myr before present at paleo-depths of 5–6 km (Omar et al., 2003). Present-day temperatures at depths of several km were established in these rocks by ~ 30 Myr BP. Local variations in thermal gradients past and present resulted from groundwater advection (Omar et al., 2003).

Earlier studies showed several lines of evidence for a significant microbial component to the CH₄ gas from the Beatrix and Masimong mines and archaea are documented at the Beatrix, Masimong, and Tau Tona sites (Ward et al., 2004; Simkus et al., 2016). For the Beatrix and Masimong sites, low $\delta^{13}\text{C}$, moderate δD , and relatively high C1/C2+ (i.e., CH₄/(C₂H₆ + C₃H₈ + ...)) all point to dominantly microbial methane mixed with a minor non-microbial end-member (Ward et al., 2004). In contrast, gases from the Kloof and Tau Tona mines may represent mixtures between methane produced by subsurface microbial communities and abiotic methane produced by water–rock reactions fed by mM concentrations of dissolved H₂ in the older, deeper systems (Sherwood Lollar et al., 2006, 2008). Methane from both mines exhibit higher $\delta^{13}\text{C}$ values and lower δD values, suggesting less of a microbial component at these sites than at the Beatrix and Masimong mines. What is more, no evidence for methanogens was found in Kloof mine samples (Kieft et al., 2005). In general, deeper, more saline and chemically evolved waters in the mines are associated with low biodiversity chemoautotrophic microbial communities isolated from the surface (Lin et al., 2006; Lippmann-Pipke et al., 2011), suggesting that there might be an inverse correlation between the microbial component of CH₄ and the antiquity of the waters.

Methane gases from two mines from the Canadian Shield were analyzed in this study. As in the case of the South African gold mines, methane from these localities is dissolved in saline groundwaters isolated within fracture systems in the rocks. The two sites were selected for this study because they appear to represent distinct methane end-members for these fracture fluid systems, one dominantly microbial in origin and the other mainly abiotic in origin. Gas is sampled upon depressurization into the mine through boreholes and seeps using methods described by Ward et al. (2004) and Sherwood Lollar et al. (2006).

The Kidd Creek mine is within one of the world's largest volcanogenic massive sulfide deposits and, extending from the surface to a depth of 3 km, it is also one of the world's deepest working mines. It is located in the southern volcanic zone of the Abitibi greenstone belt (2700 Ma), north of Timmins Ontario, Canada (Fig. 4). Kidd Creek is the most extensively studied locality in our data set. Some sample sites at Kidd Creek have been monitored continuously for a decade or more ever since an abiotic origin for methane in the mine at the 6800 foot level (2072 m) was first proposed (Sherwood Lollar et al., 2002). Since that time, fluids have been studied from all levels down to the current operating depth of 9800 feet (2987 m). The deepest, most saline fluids in the mine have billion year residence times deduced from dissolved noble gases, some of which may be vestiges of Archean atmosphere (Holland et al., 2013).

Data are presented from samples collected at two levels in the mine (7850 and 9500 feet) and collected over a period of 8 years. Measured water temperatures at depths corresponding to the samples used here are about 23 °C to 26 °C at the 7850 level and 29 °C to 32 °C at the 9500 level. The Kidd Creek gas is considered to be an example of low-temperature abiotic methane in part by virtue of its low bulk δD values, relatively high $\delta^{13}\text{C}$ values, low CH₄/C₂+, the $^{13}\text{C}/^{12}\text{C}$ ratios of associated ethane, propane, and butane, and crustal, as opposed to mantle, $^3\text{He}/^4\text{He}$ (Sherwood Lollar et al., 2006).

Birchtree is a nickel mine located in Manitoba, Canada and is part of the same property as the Thompson mine. It lies within the Circum-Superior Belt igneous province (Fig. 4). The sample used in this study was sampled at a depth of 1200 m. Water temperatures are 20–22.5 °C. The sample was selected because the methane from this locality is thought to be largely the product of microbial methanogenesis.

3.4. Shale gas

Nominally thermogenic gases are represented in this study by samples of the Utica and Marcellus shales from the Appalachian Basin of the eastern United States (Fig. 4). The Marcellus Shale is a black carbonaceous shale of Middle Devonian age occurring at a maximum depth of about 1.6 km beneath the states of Pennsylvania, New York and West Virginia, United States, rising to shallower depths westward into the neighboring state of Ohio. The sample used in this study is from a Shell well from central Pennsylvania. The Utica Shale lies hundreds of meters to ~ 2 km beneath the Marcellus and comprises organic-rich calcareous black shale of Middle Ordovician age (Rowan, 2006). The sample used here is also from central Pennsylvania. Methane exists in low-permeability pore space and in fractures (both units are unconventional economic gas sources). The gases are generally agreed to be thermogenic in origin (Jenden et al., 1993). Present-day temperature at the maximum depth of the Marcellus Shale is about 60 °C while at the maximum depth of the Utica Shale it is about 90 °C (Rowan, 2006). Modeling of the thermal history of the Appalachian Basin in general suggests that the lower units experienced maximum temperatures of 250 to as high as

300 °C (Burruss and Laughrey, 2010). Thermal modeling described briefly by Stolper et al. (2014a) in a supplement suggests that the Marcellus Shale experienced maximum burial 270 Myr before present with maximum temperatures of ~180 °C and methane generation at 173 °C. The thermal histories of these rocks are complicated by burial metamorphism following Alleghanian thrust faulting. Burruss and Laughrey (2010) suggest that mixing of gases with disparate $^{13}\text{C}/^{12}\text{C}$ and D/H has occurred for Utica gases, perhaps resulting in reverse isotope effects in which $\delta^{13}\text{C}$ (CH_4) > $\delta^{13}\text{C}$ (C_2H_6) > $\delta^{13}\text{C}$ (C_3H_8) > $\delta^{13}\text{C}$ (C_4H_{10}). Minor extant microbial activity has been documented in the Marcellus wells in Pennsylvania, including low abundances of halotolerant methanogens (Cluff et al., 2014).

A sample from the Beecher Island gas field of the Denver Basin, Yuma County, Colorado (Fig. 4) was provided to us by the U.S. Geological Survey for analysis. The gas derives from the Cretaceous Niobrara Formation at a depth of ~500 to 550 m (Lockridge, 1977). Although thermogenic gases are produced elsewhere in the Niobrara at greater depths, methane from this relatively shallow depths has been classified as “biogenic” (implying microbial) in origin (Lehr and Keeley, 2016).

3.5. FTT synthesis of CH_4 at low temperatures

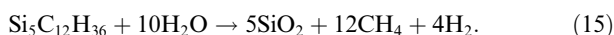
We analyzed gases produced by the Sabatier reaction:



catalyzed by ruthenium (Ru) using methods described by Etiope and Ionescu (2015). These experiments are meant to simulate the production of methane at relatively low temperatures in serpentinized ultramafic rock environments. In brief the reaction proceeded in borosilicate glass Wheaton bottles filled with ~5 ml of CO_2 and 50 ml of H_2 diluted with Ar as a makeup gas. The metal catalyst was ~3 g of 3.8% Ru on alumina support (Ru mainly in the form of RuO_2 as it may occur in natural chromites). Bottles were held in a temperature-controlled oven at 70 °C (up to 210 h) and 90 °C (for 30 days).

3.6. $\text{Si}_5\text{C}_{12}\text{H}_{36}$ decomposition experiments

A series of cold-seal experiments was conducted at the Geophysical Laboratory to constrain kinetic and equilibrium $\Delta^{12}\text{CH}_2\text{D}_2$ and $\Delta^{13}\text{CH}_3\text{D}$ effects of methane production at high temperatures (300–600 °C) and pressures (100 MPa) (Table 1). In these experiments $\text{Si}_5\text{C}_{12}\text{H}_{36}$ (tetraakis(trimethylsilyl) silane) reacts with H_2O to produce SiO_2 (s), CH_4 and H_2 :



By this reaction CH_4 is produced by CH_3 escape from the silane structure followed by addition of hydrogen. The samples consisted of H_2O (~50 mg) and $\text{Si}_5\text{C}_{12}\text{H}_{36}$ (~3 mg, Alfa Aesar 98% – natural D/H abundance) along with a roughly 2 mg mixture of Ni (Alfa Aesar, Puratronic 99.996%, <10 μm diameter grain) and Pt metals (100 μm \times 70 μm OD rod) with no specific in-plane crystal orientation (e.g. Ni(111), Pt(111)). Reaction times were

from 286 (600 °C) to 453 (300–500 °C) h. Previous in-situ and real-time observations have shown that complete decomposition of $\text{Si}_5\text{C}_{12}\text{H}_{36}$ occurs within as little as 5 min at 600 °C (Foustoukos and Mysen, 2013). In the current study, the experimentally produced CH_4 ranged from 104 to 194 μmole .

Reactants were placed in 2.5-cm long, 5-mm OD Au capsules. The Au tubes were annealed at 900 °C, boiled in 6 N nitric acid and finally cleaned with deionized water prior to use. The capsules were welded shut by a tungsten inert-gas high-frequency pulse welder that generates very low heat output, preventing H_2O volatilization (weight loss <0.1 wt%). The experimental charges were hosted in ~30 ml pressure vessels (Tuttle, 1949; Frantz et al., 1992) to minimize the quench times. Quenching was by immersion in a water bath. The average cooling rate is approximated to 100 °C/s between 600 °C and 100 °C. Immediately after cooling, capsules were weighed to check for leakage. Temperatures were recorded by sheathed chromel–alumel thermocouples placed in contact with the pressure medium (H_2O) (± 1 °C). Pressure was monitored to ± 0.1 MPa by a Heise ST-2H digital gauge that is factory-calibrated.

Product gases were sealed in borosilicate breakseal tubes for shipment to UCLA. The breakseals were opened to the vacuum extraction system for isolation of CH_4 .

3.7. Isotope exchange experiments

We used the intra-species exchange of isotopes for methane gas as a means of verifying the accuracy of our measurements. Methane gas was sealed in borosilicate or quartz breakseal tubes together with platinum on alumina. Breakseals were placed in a temperature-controlled tube furnace for 72 h to a week. The breakseals were quenched in water or air and the gases released by cracking the glass directly into the purification vacuum line.

3.8. Methanogens in the laboratory

Isotope ratios for methane produced by three methanogen species and two substrates are reported here. The axenic cultures were grown at the University of Southern California in 100–160 ml crimped serum bottles. The carbon source is either 125 mM methanol or CO_2 dissolved in water. Conversion rate from methanol is ~75%. The data reported here include methane produced by *Methanosarcina barkeri* grown at 30 °C by the reaction $4\text{CH}_3\text{OH} \rightarrow 3\text{CH}_4 + \text{CO}_2 + 2\text{H}_2\text{O}$, *Methanosarcina acetivorans* at 30 °C by the reaction $4\text{CH}_3\text{OH} \rightarrow 3\text{CH}_4 + \text{CO}_2 + 2\text{H}_2\text{O}$, and *Methanothermococcus thermolithotrophicus* grown at 65 °C by the reaction $\text{HCO}_3^- + 4\text{H}_2 + \text{H}^+ \rightarrow \text{CH}_4 + 3\text{H}_2\text{O}$. CH_4 was extracted from the serum bottles using a gas-tight syringe and injected into the vacuum line for purification.

3.9. Microbial communities in Precambrian craton fracture waters

In order to characterize the archaeal community composition in the fracture water from the Beatrix, Masimong,

Table 1

Isotope ratio data for CH₄ collected as part of this study together with isotope ratio data for coexisting H₂ and H₂O and calculated inter-species temperatures. All delta values and their uncertainties are given in ‰.

	Days since hole drilled	$\delta^{13}\text{C}_{\text{CH}_4}$ (VPDB)	$\pm 1\text{se}$	$\delta\text{D}_{\text{CH}_4}$ (VSMOW)	$\pm 1\text{se}$	$\Delta^{13}\text{CH}_3\text{D}$	$\pm 1\text{se}$	$\Delta\text{CH}_2\text{D}_2$	$\pm 1\text{se}$	Vol % H ₂	$\delta\text{D}_{\text{H}_2}$ (VSMOW)	$\delta\text{D}_{\text{H}_2\text{O}}$ (VSMOW)	CH ₄ /H ₂ T°C, Horibe & Craig (1995)	CH ₄ /H ₂ T°C, Bottinga (1969)	H ₂ OL/H ₂ T°C, Horibe & Craig (1995)
<i>Canadian Shield</i>															
Kidd Creek 7850 12287A 19.09.2013	2334	-41.404	0.004	-389.52	0.02	5.34	0.11	14.86	0.29	5.74	-739	-35.68	83.91	114	30
Kidd Creek 7850 12299 02.04.2014	2500	-39.644	0.003	-391.46	0.02	5.75	0.10	17.98	0.27	2.62	-736	-34.42	88.20	118	33
Kidd Creek 7850 12261 22.10.2015	3087	-38.735	0.013	-411.67	0.02	5.81	0.08	16.39	0.30	3.07		-33.43			
Kidd Creek 7850 12287A 02.04.2014	2529	-41.858	0.003	-391.54	0.02	5.03	0.12	14.03	0.32	3.69	-734		90.48	121	
Kidd Creek 9500 13762 14.06.2012	99	-32.598	0.003	-422.25	0.02	5.58	0.08	-6.27	0.25	17.08	-717	-29.31	127.73	160	44
Kidd Creek 9500 13684 14.06.2012	177	-32.147	0.014	-429.34	0.01	5.76	0.09	-9.91	0.24	12.15	-717	-30.89	132.20	165	44
Kidd Creek 9500 13762 16.01.2013	315	-35.919	0.016	-421.25	0.02	6.00	0.07	5.25	0.29	0.34	-714	-77.28	130.91	164	56
Kidd Creek 9500 BH2 28.11.2012	334	-32.709	0.005	-420.75	0.02	5.19	0.13	-6.34	0.31	15.24	-708		138.27	172	
Kidd Creek 9500 13762 16.01.2013 (2)	315	-34.300	0.005	-419.85	0.02	5.37	0.11	4.05	0.33	0.34	-714		130.03	163	
Kidd Creek 9500 BH2 16.01.2013	381	-31.787	0.004	-420.01	0.02	5.26	0.12	-8.45	0.31	15.57	-714	-28.37	130.13	163	45
Birchtree 3900 9167 06.11.2007		-49.736	0.012	-343.93	0.01	6.05	0.17	21.61	0.29						
<i>Witwatersrand Basin</i>															
Masimong MM51940FW 29.06.2012		-58.921	0.003	-216.60	0.04	6.10	0.15	13.58	0.47	0.01		-40.06			
Beatrix BE326FW 07.12.2011		-53.512	0.024	-206.39	0.02	6.49	0.12	13.90	0.44	0.01		-41.36			
Kloof KL445FW 19.07.2011		-36.167	0.015	-323.67	0.02	3.13	0.11	15.43	0.33	0.01		-30.34			
Tau Tona 109FW 08.02.2012		-41.096	0.007	-367.06	0.02	5.14	0.10	2.98	0.39	0.01		-25.29			
Tau Tona 107FW 08.11.2011		-41.932	0.007	-359.77	0.02	4.95	0.09	4.25	0.32	0.01					
Chimaera G1		-12.644	0.003	-121.07	0.02	3.59	0.13	8.45	0.65		-720 [†]		13.12	43	
Chimaera G2		-14.630	0.003	-122.25	0.01	3.26	0.11	10.24	0.42		-720 [†]		13.39	43	
Chimaera G3		-12.493	0.004	-120.83	0.01	3.49	0.13	9.02	0.38		-720 [†]		13.07	43	
Cabeco de Vide		-23.977	0.010	-282.63	0.06	3.32	0.01	-7.57	0.34						
Acquasanta Terme	3500	-9.477	0.005	-251.56	0.02	1.86	0.01	15.80	0.34						
<i>Thermogenic gases</i>															
Beecher Island field, Denver Basin		-61.572	0.035	-219.82	0.01	3.23	0.12	5.51	0.41						
Marcellus Shale		-36.449	0.005	-158.31	0.01	3.11	0.09	9.33	0.44						
Utica Shale		-25.969	0.007	-154.00	0.02	3.05	0.12	9.25	0.41						
<i>Microbial CH₄ in the laboratory</i>															
<i>Methanosarcina acetivorans</i> , 30 °C		-32.768	0.007	-328.41	0.02	-3.88	0.20	-40.86	0.36						
<i>Methanosarcina acetivorans</i> , 30 °C		-32.763	0.005	-328.45	0.02	-3.84	0.09	-43.24	0.31						
<i>Methanosarcina barkeri</i> , 30 °C		-56.550	0.007	-340.18	0.02	-1.11	0.13	-34.33	0.35						
<i>Methanococcus thermolithotrophicus</i> , 65 °C		-49.355	0.011	-394.37	0.02	2.66	0.10	-19.44	0.30						
<i>Abiotic CH₄ in the laboratory</i>															
Sabatier reaction, 90 °C		-37.393	0.000	-434.02	0.29	4.20	0.52	-55.86	2.01						
Sabatier reaction, 70 °C		-43.095	0.012	-417.80	0.04	3.08	0.17	-53.69	0.54						
Si ₅ C ₁₂ H ₃₆ + H ₂ O 600 °C		-48.567	0.007	-134.41	0.02	0.62	0.14	1.41	0.50						
Si ₅ C ₁₂ H ₃₆ + H ₂ O 600 °C		-48.548	0.011	-155.72	0.02	0.52	0.22	0.37	0.46						

Si ₅ C ₁₂ H ₃₆ + H ₂ O 600 °C, not catalyzed	-49.772	0.009	-157.06	0.01	0.04	0.12	0.74	0.40
Si ₅ C ₁₂ H ₃₆ + H ₂ O 500 °C	-50.657	0.004	-230.27	0.02	-0.18	0.11	-4.79	0.409
Si ₅ C ₁₂ H ₃₆ + H ₂ O 500 °C	-53.882	0.014	-271.80	0.02	0.74	0.16	-9.20	0.45
Si ₅ C ₁₂ H ₃₆ + H ₂ O 400 °C	-49.197	0.004	-185.75	0.02	0.30	0.13	-2.28	0.47
Si ₅ C ₁₂ H ₃₆ + H ₂ O 400 °C, not catalyzed	-49.063	0.012	-246.19	0.01	1.08	0.15	-3.04	0.34
Si ₅ C ₁₂ H ₃₆ + H ₂ O 300 °C	-51.205	0.008	-248.85	0.01	0.50	0.14	-7.64	0.39
<i>Equilibration on Pt</i>								
UCLAI 500C ± 5 °C	-40.401	0.003	-79.41	0.02	0.74	0.14	1.81	0.50
UCLAI 300 ± 10 °C	-37.013	0.005	-106.90	0.01	1.70	0.16	3.17	0.43
UCLAI 400C ± 5 °C	-37.353	0.003	-86.60	0.02	1.28	0.10	1.94	0.46
UCLAI 500C ± 5 °C	-37.767	0.010	-69.16	0.02	0.99	0.12	0.96	0.55
UCLAI 400C ± 5 °C	-37.099	0.003	-93.81	0.01	1.10	0.11	2.04	0.46

† Etiopo et al. (2011).

and Tau Tona mine boreholes, the V6 hypervariable region of the archaeal 16S rRNA gene was amplified and sequenced as described in Simkus et al. (2016). A 100% overlap quality filter was applied to the V6 paired end sequences and clustered using the Minimum Entropy Decomposition (MED) pipeline (-A 0 -M 2 -d 4) (Eren et al., 2015). Sequences that passed quality control and the MED pipeline were annotated using GAST (Huse et al., 2008) and a GAST formatted V6 reference set (https://vamps.mbl.edu/data_downloads/refv6a.tgz).

3.10. Gas purification

We purify methane gas for isotopic analysis on a vacuum line interfaced with a gas chromatograph (GC). Samples are delivered to the vacuum line through a septum by either gas-tight syringe or with an 18 gauge needle attached to the line with a dedicated small-volume valve (SGE SMOV). The vacuum line is composed of 316 L tubing connected with VCR face seal fittings (Swagelok) and Conflat CF flanges. It is hydrocarbon free, consisting of a turbo-molecular pump backed by a diaphragm rough pump. Sample gases are trapped on silica gel at liquid-N₂ temperature. Helium carrier gas is then used to flush the sample gas from the silica gel trap to the GC while warming the trap to ~30 °C. Carbon dioxide is retained on silica gel at room temperatures and is lost from the sample after warming the first trap. Purified methane exiting the GC is trapped on a second silica gel trap at liquid-N₂ temperature for 30 min. After slowly purging the trap of He the sample is transferred to an evacuated sample tube filled with silica gel. This tube is used to introduce the sample to the dual inlet of the mass spectrometer by expansion while heating the silica gel to 60 °C. Samples are mixed during expansion from the sample tube into the variable-volume bellows of the instrument for 20–40 min depending upon the size of the bellows used and the sample quantity. Mixing is promoted by squeezing and expanding the variable-volume bellows and by applying freeze/thaw cycles on the silica gel. Mixing ensures isotope fidelity when expanding from the sample tube to the variable volume of the instrument.

Two GC columns are used in series for purification. The first is a 3-meter 1/8 inch OD stainless steel (SS) column packed with 5A molecular sieve. This is followed by a 2-meter 1/8 inch OD SS column packed with HayeSep D porous polymer. Flow rate of the He carrier gas is 20 ml/min and the columns are held at a fixed temperature of 25 °C during sample processing. The first column separates H₂, Ar, O₂ and N₂ from methane and other hydrocarbons. The second column separates CH₄ from C₂H₆, C₃H₈ and higher order hydrocarbons. Peaks are identified using a passive TCD detector. Retention times of base-line resolved methane are ~17 ± 1 min under these conditions. Thirty-minute collection times ensure capture of all of the eluting methane peak tail with isotope fidelity.

3.11. Mass spectrometry

We measured ion currents of ¹²CH₄⁺, ¹³CH₄⁺, ¹²CH₃D⁺, ¹³CH₃D⁺ and ¹²CH₂D₂⁺ for methane gas samples using the

prototype Panorama (Nu Instruments) high-mass-resolution gas-source multiple collector mass spectrometer. Details surrounding the measurement of methane gas with this instrument were reported previously (Young et al., 2016). Here we summarize the measurement procedures. The reader is referred to Young et al. (2016) for a comprehensive description of the mass spectrometer and methods.

The instrument is set to a mass resolving power (MRP) of $\sim 40,000$ or greater (instrumental $M/\Delta M$ where ΔM is defined at 5 and 95% peak heights) with an entrance slit width of $\sim 35 \mu\text{m}$. At this resolution the two mass-18 rare isotopologues are effectively resolved (Fig. 5). Mass 16 and mass 17 isotopologues are measured using Faraday collectors with amplifier resistors of $10^{11} \Omega$. Both mass-18 isotopologues are measured with an electron multiplier as the axial collector. Isotopologue ratios are obtained using two magnet current settings (Fig. 5). In the first setting, the magnet is set to place $^{13}\text{CH}_3\text{D}^+$ (mass = 18.04090 amu) in the axial collector and ratios of $^{13}\text{CH}_4^+ / ^{12}\text{CH}_4^+$ and $^{13}\text{CH}_3\text{D}^+ / ^{12}\text{CH}_4^+$ are obtained. $^{13}\text{CH}_3\text{D}^+$ is measured at a count rate of $\sim 6,000$ to 10,000 cps (depending upon sample size). Twenty blocks composed of twenty 30-s integration cycles are used for these ratios. In the second setting, the magnet current is shifted to place $^{12}\text{CH}_2\text{D}_2^+$ (mass = 18.04385 amu) in the axial collector. In addition, the continuously variable collector slits are adjusted to bring the $^{12}\text{CH}_4^+$ beam into coincidence with the mass-17 and mass-18 beams (only the slit is migrated across the major beam, collectors remain in fixed position). In this setting $^{12}\text{CH}_3\text{D}^+ / ^{12}\text{CH}_4^+$ and $^{12}\text{CH}_2\text{D}_2^+ / ^{12}\text{CH}_4^+$ are measured (Fig. 5). Typical count rates for measurements of $^{12}\text{CH}_2\text{D}_2^+$ are ~ 200 to 300 cps. Forty blocks of twenty 30-s integrations are used for these ratios. A 25 ns dead-time correction, although unnecessary at the count rates used, is applied to the electron multiplier. The sample and reference gas bellows are adjusted to balance the ion current intensities between each measurement cycle, enabling long-duration measurements.

Internal precision is consistent with counting statistics, yielding typical measurement uncertainties of $\pm 0.15\%$

and $\pm 0.35\%$ 1se for $\Delta^{13}\text{CH}_3\text{D}$ and $\Delta^{12}\text{CH}_2\text{D}_2$, respectively. Measurement uncertainties for $\delta^{13}\text{C}$ (VPDB) and δD (VSMOW) are typically 0.003 and 0.02‰ 1se, respectively. The accuracy of these methods has been assessed using inter-laboratory comparisons and the mixing experiments shown in Fig. 2 (Young et al., 2016). In addition to these previous assessments, we report here measurements of gases equilibrated at known temperatures in order to demonstrate further the accuracy of $\Delta^{13}\text{CH}_3\text{D}$ and $\Delta^{12}\text{CH}_2\text{D}_2$ measurements relative to theory (Section 4.1). External 1σ precision for $\delta^{13}\text{C}$, δD , $\Delta^{13}\text{CH}_3\text{D}$, and $\Delta^{12}\text{CH}_2\text{D}_2$ is approximately 0.1‰, 0.2‰, 0.2‰ and 0.6‰, respectively, based on replicate samples.

4. LABORATORY STUDIES

4.1. Isotope exchange experiments – assessing accuracy

The accuracy of our measurements was initially assessed through mixing experiments and inter-laboratory comparisons (Young et al., 2016). Because there are at the time of this writing no other data for CH_2D_2 at natural abundances, further assessment is justified. We addressed the accuracy in both $\Delta^{12}\text{CH}_2\text{D}_2$ and $\Delta^{13}\text{CH}_3\text{D}$ by analyzing products of the heating experiments in which intra-species equilibration by isotope exchange is promoted by both temperature and the presence of a platinum catalyst (Table 1). Our results are compared with theory (Eqs. (12) and (13)). Fig. 6 shows the results for $\Delta^{13}\text{CH}_3\text{D}$ vs. equilibration temperature. Methane synthesis experiment products were included in the plot as well. The high-temperature catalyzed silane reaction products (600 °C) and the platinum-catalyzed equilibration experiments are all within analytical uncertainties of the theoretical relationship between $\Delta^{13}\text{CH}_3\text{D}$ and T ; the equilibration experiments match theory. The 90 °C Sabatier reaction product also matches the theory curve although it could be argued that this datum should be excluded because the gas is grossly out of equilibrium in $\Delta^{12}\text{CH}_2\text{D}_2$ (see below). Indeed the lower-temperature 70 °C reaction product is far from expected

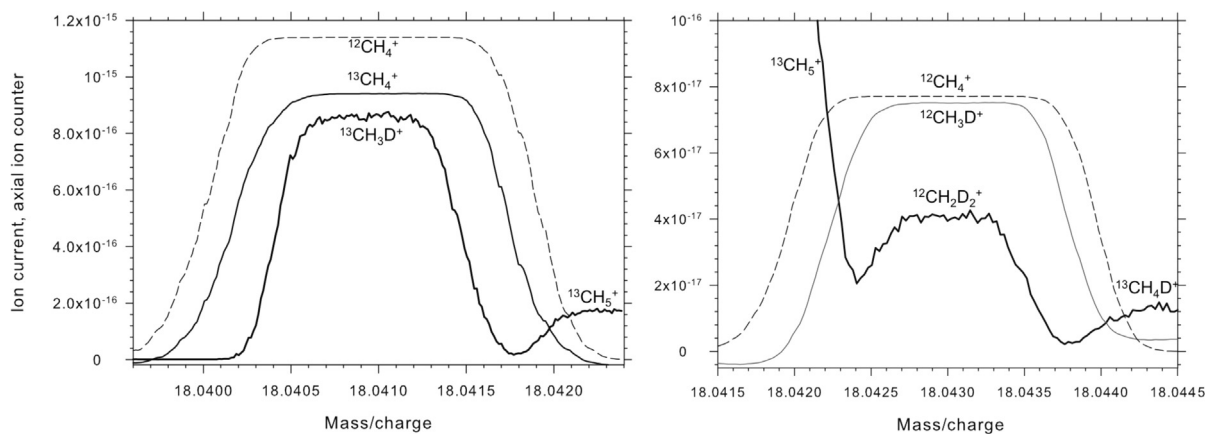


Fig. 5. Mass spectrometry peak shapes for methane gas obtained using the analytical methods used in this study. Left: magnet current and collector slit settings for analysis of $\delta^{13}\text{C}$ and $\Delta^{13}\text{CH}_3\text{D}$. Right: settings for analysis of δD and $\Delta^{12}\text{CH}_2\text{D}_2$. The ordinate values are ion currents for the axial ion counter in amps. The abscissa units are daltons/unit charge (thomsons). Ion counter peak shapes are averages of 20 individual scans. Mass-17 and mass-16 peaks are scaled for direct comparison with the axial mass-18 beam currents.

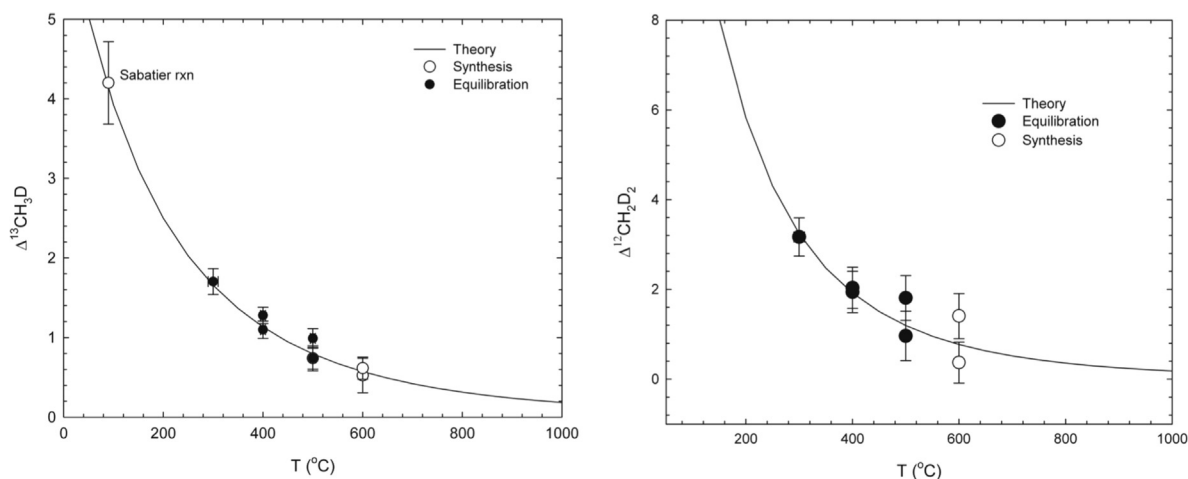


Fig. 6. Plots of catalyzed CH_4 intra-species isotope exchange experiments (black symbols) and high-temperature CH_4 abiotic synthesis experiments (open symbols) compared with the theoretical relationships between $\Delta^{13}\text{CH}_3\text{D}$ vs. T (left) and $\Delta^{12}\text{CH}_2\text{D}_2$ vs. T (right).

equilibrium in $\Delta^{13}\text{CH}_3\text{D}$ as well as in $\Delta^{12}\text{CH}_2\text{D}_2$. Similarly, measured $\Delta^{12}\text{CH}_2\text{D}_2$ values from the catalyzed exchange experiments and the 600 °C silane reaction products agree with the theoretical relationship between $\Delta^{12}\text{CH}_2\text{D}_2$ and T (Fig. 6).

4.2. Abiotic synthesis experiments – the $^{12}\text{CH}_2\text{D}_2$ signature of abiotic methane synthesis

Results of the Sabatier reaction experiments and the $\text{Si}_5\text{-C}_{12}\text{H}_{36}$ decomposition experiments are shown in Fig. 7 and listed in Table 1. While the experiments differ in detail, the overall pattern that emerges is one in which large deficits in $^{12}\text{CH}_2\text{D}_2$ relative to equilibrium and rather smaller deficits in $^{13}\text{CH}_3\text{D}$ relative to equilibrium typify abiotic methane formation in the laboratory. In fact, $\Delta^{13}\text{CH}_3\text{D}$ values are broadly consistent with the temperatures of formation although as a rule precise temperatures are not faithfully recorded at $T < 600$ °C. The Sabatier reaction run at 90 °C shows a deficit in $^{12}\text{CH}_2\text{D}_2$ but the $\Delta^{13}\text{CH}_3\text{D}$ value is consistent with the methane formation temperature within analytical uncertainties (Fig. 6). However, at 70 °C, the $\Delta^{13}\text{CH}_3\text{D}$ value is too low by about 1‰. At 300–400 °C values for $\Delta^{12}\text{CH}_2\text{D}_2$ in the gases produced by silane decomposition are still low by many per mil compared with equilibrium and $\Delta^{13}\text{CH}_3\text{D}$ values are low by typically ~1‰ relative to equilibrium. Two silane decomposition experiments were conducted in the absence of a metal catalyst, and in both cases $\Delta^{13}\text{CH}_3\text{D}$ values are lower than with the catalyst at the same temperatures by ~1/2‰ (Table 1). In Section 4.4 we investigate the causes of this overall pattern of kinetic isotope effects.

4.3. Methanogens in the laboratory

Methane produced by axenic *M. barkeri* and *M. acetivorans* at 30 °C by the reaction $4\text{CH}_3\text{OH} \rightarrow 3\text{CH}_4 + \text{CO}_2 + 2\text{H}_2\text{O}$, and *M. thermolithotrophicus* grown at 65 °C by the reaction $\text{HCO}_3^- + 4\text{H}_2 + \text{H}^+ \rightarrow \text{CH}_4 + 3\text{H}_2\text{O}$

all show marked kinetic isotopologue effects. Relatives of these methanogens have been identified in the South African mines of this study. In each of the three experiments deficits in $^{12}\text{CH}_2\text{D}_2$ comparable in magnitude to those produced in the abiotic experiments are observed (Fig. 8). At 30 °C, the kinetically-controlled deficits in $^{13}\text{CH}_3\text{D}$ of up to 10‰ are more extreme than those observed in the abiotic experiments. Negative $\Delta^{12}\text{CH}_2\text{D}_2$ values are evidently characteristic of microbial methane produced in the laboratory under favorable conditions for methanogen growth.

Previous work on $\Delta^{13}\text{CH}_3\text{D}$ values in microbially-produced methane has identified instances of equilibrium or near-equilibrium $\Delta^{13}\text{CH}_3\text{D}$ values as well as instances of kinetic control like that shown in the cultures presented here (Stolper et al., 2015; Wang et al., 2015). Our results show that kinetic depletions in $^{13}\text{CH}_3\text{D}$ are accompanied by even larger deficits in $^{12}\text{CH}_2\text{D}_2$ relative to equilibrium.

4.4. Kinetic signatures of CH_4 formation – the role of quantum tunneling

In order to gain some understanding of the kinetic effects associated with abiotic methane production, a reaction network representing the formation of methane on metal surfaces was constructed (Fig. 9). We used the reaction scheme for FTT synthesis on a cobalt (Co) catalyst suggested by Qi et al. (2014). While we use CO as the source of carbon because the elementary steps in this reaction are well studied, methanation of CO_2 can occur by conversion first to CO with the subsequent steps being the same as those for direct methanation of CO (Wang et al., 2011). The kinetic model presented here is therefore relevant to methane production from CO_2 as well. We added isotope exchange between methane molecules on the surface, desorption and adsorption of CH_4 gas, and attack of CH_4 by OH to the elementary steps leading to methane formation. The set of reactions can be represented by these basic reactions and their isotopically-substituted equivalents:

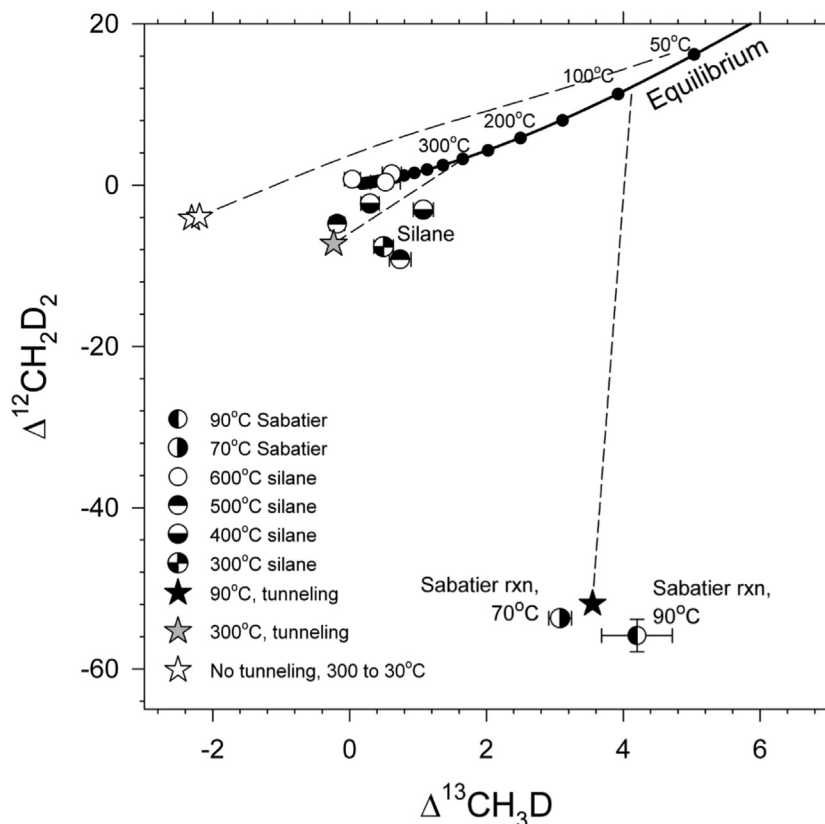
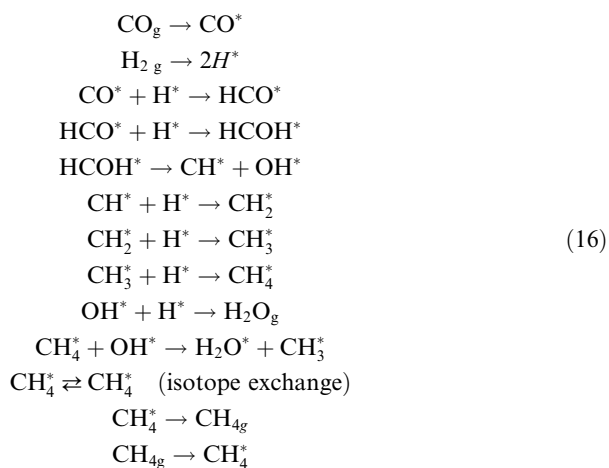


Fig. 7. Plot of $\Delta^{12}\text{CH}_2\text{D}_2$ and $\Delta^{13}\text{CH}_3\text{D}$ values for methane gases produced abiotically in the laboratory by the Sabatier reaction and the hydrolysis of silane. Also shown are results of kinetic models for the isotopic effects of metal-catalyzed abiotic methane formation described in the text. Open stars show the results of classical kinetics. The black (90 °C) and grey (300 °C) stars show the results that include quantum tunneling. Dashed lines show the calculated evolution paths towards equilibrium for each kinetic model. The equilibrium curve is shown for reference.



where a superscript * signifies a surface-adsorbed species and a subscript g refers to a gas species. With all isotopologues and isotopomers the model consists of 124 species and 796 reactions. The rate constants for the reactions are of the form

$$k_f = Q_{\text{Tun}} \frac{k_b T}{h} \frac{q^+}{\prod_r q_r} \left(\frac{-E_a}{k_b T} \right) \tag{17}$$

where k_b is the Boltzmann constant, h is the Planck constant, E_a is the activation energy, q_r are the partition functions for reactant species r , q^+ is the partition function for the transition state, and Q_{Tun} is a correction for quantum tunneling. The 124 ordinary differential equations comprising the model were solved numerically using the Lawrence Livermore ordinary differential equation solver (DLSODE). Activation energies for the methane formation reactions were taken from Qi et al. (2014). Values for E_a for the reaction $\text{CH}_4 + \text{OH}$ were taken from Haghnegahdar et al. (2015).

Pre-exponential terms in Eq. (17) are dominated by the translational partition functions. We therefore used the 2D or 3D translational partition functions

$$\frac{q}{l^D} = \left(\frac{2\pi k_b T}{h^2} \right)^{D/2} \tag{18}$$

as appropriate to estimate the pre-exponential terms for Eq. (17) (Baetzold and Somorjai, 1976) where D is 2 for surface species and 3 for species in the gas phase and l is the length dimension. In the absence of detailed information about all of the transition states involved in the reaction network, we used the sum of the masses of the reactants as an estimate for the transition states, a method known to give reasonable values. For example, using this scheme the H/D kinetic iso-

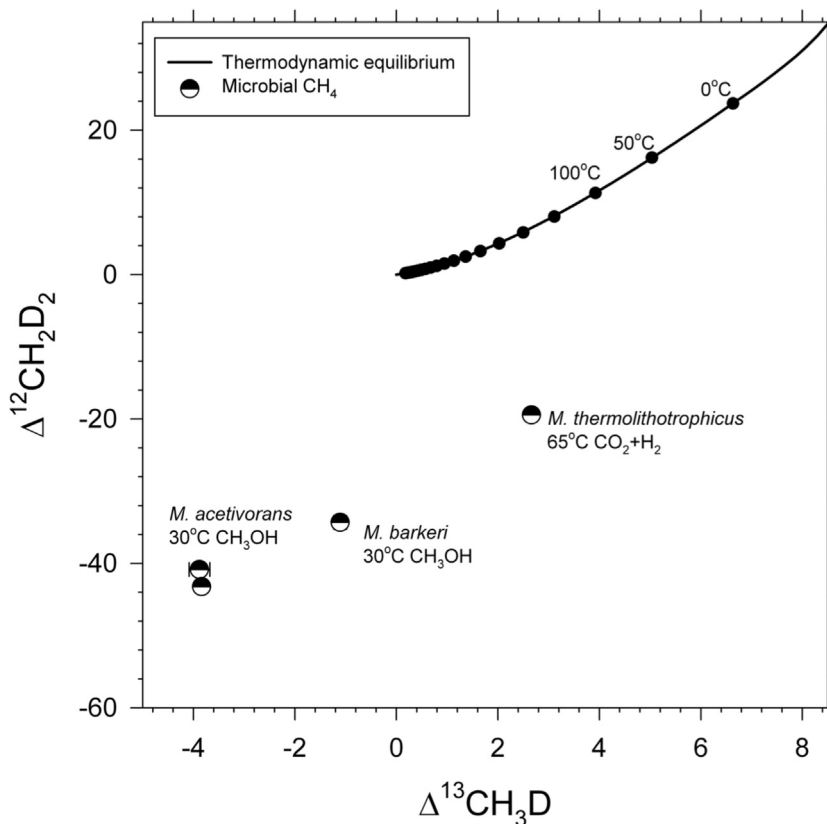


Fig. 8. $\Delta^{12}\text{CH}_2\text{D}_2$ vs. $\Delta^{13}\text{CH}_3\text{D}$ plot comparing the methane produced in the laboratory by three species of methanogenic Archaea. The equilibrium curve is shown for reference.

tope effect (KIE) obtained in our code for the reactions $\text{HCO}^* + \text{H}^* \rightarrow \text{HCOH}^*$ and $\text{HCO}^* + \text{D}^* \rightarrow \text{HCOH}^*$ is 1.98 while the value given by Qi et al. is 1.93. Similarly, for the reactions $\text{HCOH}^* \rightarrow \text{CH}^* + \text{OH}^*$ and $\text{DCOD}^* \rightarrow \text{CD}^* + \text{OD}^*$ our calculated KIE is 1.02 while that from Qi et al. is 1.004. Overall we estimate an accuracy in KIE values relative to the fiducial density functional theory calculations of ~ 2 to 5%. We note that variations in activation energies for the surface catalyzed steps in our reaction network exhibit greater ranges in the literature than our estimate in accuracy uncertainty.

In the absence of more detailed information, rate constants for isotope exchange between methane molecules on the metal surface are taken to be 10^{12} s^{-1} . The rate constant for desorption of methane is set at 10^2 s^{-1} and we did not include an isotope effect from desorption. Re-adsorption was excluded from the results presented here. The exact values for these constants do not affect the initial rate-limited isotope effects but they instead control the rate at which the methane gas progresses from kinetic to equilibrium states of isotopic bond ordering. The values used in our calculations give rates of equilibration consistent with our laboratory results.

We found that the kinetic model as described above when Q_{Tun} is unity cannot explain our experimental data for methane formation. In particular, the calculated

kinetically-controlled values for $\Delta^{13}\text{CH}_3\text{D}$ are more negative, or less positive, than our experiments and the calculated kinetic values for $\Delta^{12}\text{CH}_2\text{D}_2$ are considerably (by an order of magnitude at low temperatures) less negative than in our experiments (Fig. 7). The failure of the classical model to explain the large deficits in $^{12}\text{CH}_2\text{D}_2$ is a general result that arises because classical kinetics do not depart profoundly from the rule of the geometric mean (Bigeleisen, 1955). The latter is a rough approximation in which fractionation factors for multiply-substituted species are similar to products of fractionation factors for the corresponding singly-substituted species with the remainder being thermodynamic effects. For example, where the $^{13}\text{CH}_3\text{D}/^{12}\text{CH}_4$ kinetic fractionation factor is of order 0.999 (-1‰), one expects that the $^{12}\text{CH}_2\text{D}_2/^{12}\text{CH}_4$ fractionation effect should be roughly 0.999^2 (-2‰), and so forth (where we assume the D/H fractionation dominates over the $^{13}\text{C}/^{12}\text{C}$ fractionation). Inspection of the classical kinetic effects (open stars in Fig. 7) shows this to be approximately the case in our kinetic model. For this reason the magnitude of the classical CH_2D_2 kinetic fractionation is constrained to be on the order of a few per mil where the $^{13}\text{CH}_3\text{D}$ effect is also on the order of several per mil. This is not what we observe.

However, the de Broglie wavelength of hydrogen atoms at relevant temperatures is on the order of $1 \times 10^{-10} \text{ m}$ and

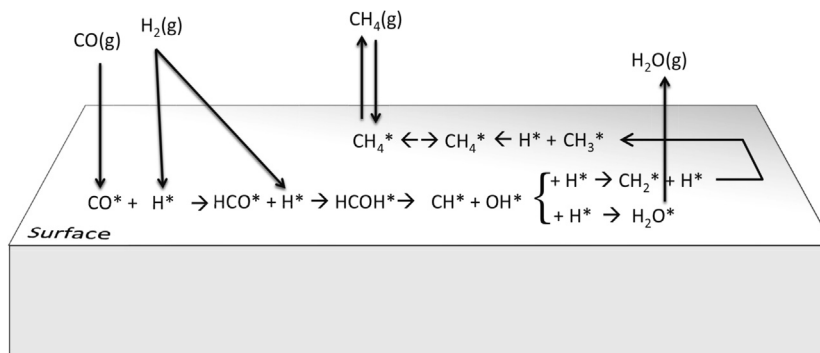


Fig. 9. Schematic showing the reaction scheme used to model the production of methane from CO and H₂ gases catalyzed on a metal surface.

the typical quantum tunneling length scale for reactions involving the C–H bond is $\sim 0.4 \times 10^{-10}$ m (Krishtalik, 2000). Tunneling should therefore be an important process affecting rate constants for the reactions involving insertion of a hydrogen or a deuterium atom. In order to add this tunneling correction we used the prescription for Q_{Tun} after Bell (1959):

$$Q_{\text{Tun}} = \frac{\alpha \exp(\alpha - \beta)}{(\alpha - \beta)} - \frac{\beta}{\alpha - \beta} \quad (19)$$

where

$$\alpha = \frac{E_a}{k_b T} \quad (20)$$

and

$$\beta = \frac{2a\pi^2(2mE_a)^{1/2}}{h} \quad (21)$$

In Eq. (21) a is the tunneling length scale (tunneling distance = $2a$, Fig. 10) and m is the mass of the tunneling particle. Eq. (19) is valid when the energy of the particle is well below the top of the energy barrier and where departures from classical behavior are relatively large (when $\alpha > \beta$) (Bell, 1980). In the present calculations $\alpha \gg \beta$.

The experimental data for methane formation by the metal-catalyzed Sabatier reaction and by silane decomposition are explained within reasonable experimental and computational uncertainties by incorporating the tunneling correction in Eq. (19) into the H and D additions in the reaction network. This fit is obtained by using $a_{\text{H}} = 0.3 \times 10^{-10}$ for H and $a_{\text{D}}/a_{\text{H}} = 1.005$. A longer tunneling length scale for D rather than H is expected (Limbach et al., 2006). Fig. 10 shows the relationships between the length scale for tunneling and activation energy in the context of a Marcus-theory representation of the reactions of interest. We note that the state of the hydrogen and deuterium atoms is not known *a priori* so the values for a_{D} and a_{H} , while accounting for the relative probabilities of tunneling for these species, may not be strictly accurate representations of the physical tunneling distances. Nonetheless, we can evaluate the plausibility of these values. For example, if we approximate the energy barrier in Fig. 10 as a parabola with the expression $(E_a - E) = f(\xi - \xi^*)^2$ where ξ is the reaction coordinate and ξ^* is the position of the barrier center, we arrive at $a = \xi - \xi^* = \sqrt{E_a/f}$ where $E = 0$ to

show that $a_{\text{D}}/a_{\text{H}} = 1.005 = \sqrt{E_a(\text{D})/E_a(\text{H})}$. The differences in activation energies represented by $a_{\text{D}}/a_{\text{H}}$ can be assessed by rewriting this relationship as $(a_{\text{D}}/a_{\text{H}})^2 = (E_a + \sqrt{m_{\text{H}}/m_{\text{D}}} \Delta E) / (E_a + \Delta E)$ where we use the square root of the inverse of the atomic masses for H and D to relate their respective energy offsets (e.g., due to zero-point energies) from a fixed activation energy barrier maximum (E_a , Fig. 10). With a typical activation energy in our reaction network of $\sim 5 \times 10^{-20}$ J (30 kJ/mol) for H or D addition and $a_{\text{D}}/a_{\text{H}} = 1.005$ we obtain $\Delta E = 0.033E_a = 1.65 \times 10^{-21}$ J. This energy corresponds to a vibrational frequency of $5 \times 10^{-12} \text{ s}^{-1}$ (170 cm^{-1}), a value that agrees with other estimates for adsorbed hydrogen to within a factor of 2 or 3 (Yu et al., 2009). The constants used in the tunneling correction appear reasonable.

The kinetic model, inclusive of tunneling, produces methane with $\delta^{13}\text{C}$ values of between -41‰ and -42‰ relative to the carbon substrate. The product methane δD values are -795‰ and -640‰ at 30 and 300 °C, respectively, relative to the reactant hydrogen. Values for δD without tunneling are closer to $\sim -550\text{‰}$. Clearly, to reproduce the δD values of natural samples, another step involving D/H isotope exchange between methane and other sources of hydrogen would have to occur. Interspecies isotope exchange before and after desorption from the metal catalyst is not included in the model at present. This exchange could explain why the depletion in $^{12}\text{CH}_2\text{D}_2$ observed in natural samples ($\sim -10\text{‰}$, see below) is not as extreme as that seen in the laboratory ($< \sim -50\text{‰}$).

With the tunneling correction the large $^{12}\text{CH}_2\text{D}_2$ depletions relative to stochastic in the experiments are explained, as are the comparatively minor departures of $^{13}\text{CH}_3\text{D}$ from equilibrium, and the overall temperature dependence in both (Fig. 7). It appears, therefore, that quantum tunneling by hydrogen is a signature of abiogenic methane production. We note that in the case of the silane decomposition reactions, the tunneling effect would be manifest in the final step where hydrogen is added to the methyl radical. The scatter in the silane decomposition data in Fig. 7 is an indication that more detailed work will be required in the future to understand the influences of temperature, catalysis, and other factors on the kinetics of this process.

The cause of the large kinetic isotopic effects in methane gas produced by methanogens under the conditions that obtained in our laboratory cultures may also involve

quantum tunneling of hydrogen (Klinman, 2003). If so, it may be possible for methanogens to produce methane with $\Delta^{12}\text{CH}_2\text{D}_2$ signatures resembling those of abiotic gas. An important distinction between the kinetic effects exhibited by CH_4 produced in our axenic laboratory cultures and CH_4 produced by abiotic reactions is that the former displays more negative $\Delta^{13}\text{CH}_3\text{D}$ values for a given $\Delta^{12}\text{CH}_2\text{D}_2$ value (compare Figs. 7 and 8). This feature of methanogenesis may indicate that tunneling is less important relative to classical kinetic effects during microbial methane production.

Alternatively, the low $\Delta^{12}\text{CH}_2\text{D}_2$ values produced by microbial methanogenesis in the laboratory could be expressions of “combinatorial” effects (Yeung, 2016). This purely statistical effect with an apparent biasing against D–D pairings would arise when the four indistinguishable hydrogen atoms comprising the product methane molecule are derived from two or more distinct isotopic reservoirs or assembled with different D/H fractionation factors, both being more likely for enzymatic processes. The magnitude of the effect scales roughly quadratically with the sizes of the disparities in isotopic ratios of the reservoirs or fractionation factors. For example, if one of the four hydrogen positions was derived from a reservoir with a D/H twice that of the others, the result would be a $\Delta^{12}\text{CH}_2\text{D}_2$ value of -40% (Rockmann et al., 2016), comparable to the values observed in the culture experiments (Fig. 8). In the case of unequal fractionation factors, if the D/H fractionation factors for four hydrogen addition steps producing CH_4 were 1.00, 1.00, 0.50 and 0.50, then the predicted $\Delta^{12}\text{CH}_2\text{D}_2$ value is -37% , also similar to the most negative

values in Fig. 8. The effect on $\Delta^{13}\text{CH}_3\text{D}$ would only be 0.01% . In general, the combinatorial effect should minimally influence $\Delta^{13}\text{CH}_3\text{D}$ values (Yeung, 2016), suggesting that these statistical effects should work against correlations between $\Delta^{12}\text{CH}_2\text{D}_2$ and $\Delta^{13}\text{CH}_3\text{D}$. The apparent correlation between $\Delta^{12}\text{CH}_2\text{D}_2$ and $\Delta^{13}\text{CH}_3\text{D}$ defined by the culture data suggest that classical kinetic effects, in addition to tunneling and/or purely statistical effects, may be playing an important role in the microbial CH_4 isotopologue signatures shown in Fig. 8.

The combinatorial effects are general and could in principle apply to abiotic as well as enzymatic formation pathways. However, the differences in fractionation factors or differences in D/H of isotopic reservoirs necessary to explain the observed negative $\Delta^{12}\text{CH}_2\text{D}_2$ values are on the order of a factor of 2. These seem to be too extreme for abiotic pathways for methane formation.

5. APPLICATIONS TO NATURAL SAMPLES

Results for all natural samples reported here are listed in Table 1. Typical methane concentrations for the gas samples can be found in the references cited in Section 3.1. The bulk isotopic compositions of the various samples are shown in Fig. 11 together with approximate boundaries for microbial, thermogenic, abiotic gas seeps, and abiotic methane discharging from ground water. The gases span typical global ranges in both $\delta^{13}\text{C}$ (VPDB) and δD (VSMOW) (Etiopie et al., 2011; Etiopie and Sherwood Lollar, 2013). Generally speaking, the isotopic compositions of the gases comport with their nominal provenance

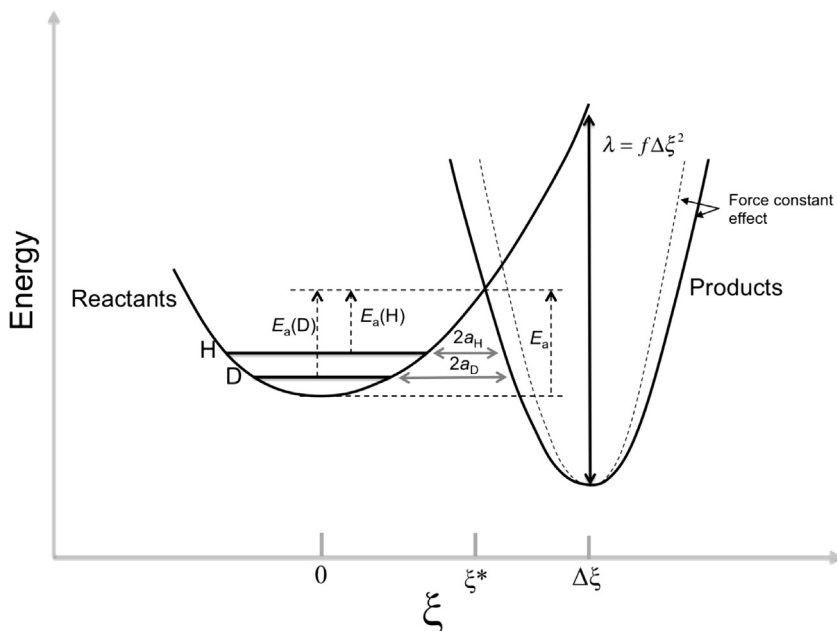


Fig. 10. Schematic illustrating the relationships between activation energy, E_a , tunneling distances for hydrogen (a_H) and deuterium (a_D) and the non-adiabatic energy parabolas representing adsorbed reactants and product. The ordinate is potential energy. The abscissa is the reaction progress coordinate ξ . Differences in tunneling distances are seen to imply corresponding differences in activation barriers for insertion of H and D atoms $E_a(\text{H})$ and $E_a(\text{D})$, respectively. $\Delta\xi$ is the separation between reactant and product energy minima that together with force constant f , controls the reorganization energy λ in the context of Marcus theory. ξ^* is the reaction coordinate position of the energy barrier for the reaction.

assignments. These same gases in $\Delta^{12}\text{CH}_2\text{D}_2$ vs. $\Delta^{13}\text{CH}_3\text{D}$ space (Fig. 12) can be broadly categorized into three groups: (1) those samples exhibiting isotopic bond ordering equilibrium, (2) those with clear negative digressions from bond-order equilibrium, and (3) those with clear positive excursions from equilibrium.

5.1. Natural samples exhibiting equilibrium – thermometry applications

A useful aspect of employing two multiply-substituted isotopologues is that the condition of intra-species equilibrium becomes immediately apparent; the temperatures derived from samples in which both $\Delta^{12}\text{CH}_2\text{D}_2$ and $\Delta^{13}\text{CH}_3\text{D}$ are consistent with equilibrium are more robust. In cases of intra-species equilibrium the need to verify the derived temperatures by comparisons with prior expectations is obviated. This is important because in many cases prior expectations for temperatures of formation are based on indirect evidence such as thermal models, assumptions of inter-species or inter-phase isotopic exchange equilibrium, or geochemical estimates for maturity, and these indicators do not always agree. Instances of intra-species equilibration are described in Sections 5.2–5.4 below.

5.2. Chimaera

Samples from Chimaera are within error (based on external reproducibility) of equilibrium (Fig. 12). The three measurements define a temperature based on $\Delta^{13}\text{CH}_3\text{D}$ of $128\text{ }^\circ\text{C} + 11/-10$ (1σ). The temperature obtained with the somewhat less precisely determined average $\Delta^{12}\text{CH}_2\text{D}_2$ is $129\text{ }^\circ\text{C} + 16/-14$ (1σ). These temperatures are significantly greater than the estimates obtained by assuming that CH_4 and H_2 gas are in hydrogen isotopic equilibrium. Using

the D/H exchange calibration of Bottinga (1969), the H_2 D/H values from Etiope et al. (2011), and the CH_4 D/H values reported here, one obtains a temperature of $43\text{ }^\circ\text{C}$ (Table 1). While the samples of H_2 and CH_4 used for the temperature calculation were not obtained at the same time, a similar result was reported by Etiope et al. (2011). Because the combination of $\Delta^{12}\text{CH}_2\text{D}_2$ and $\Delta^{13}\text{CH}_3\text{D}$ indicates intra-methane equilibrium, we interpret the discrepancy in intra-species vs. inter-species temperatures to be the result of isotopic disequilibrium between CH_4 and H_2 .

The isotopic compositions of coexisting C1–C5 alkanes, the presence of CO_2 gas and N_2 gas derived from mature organic matter, the molecular C1–C5 Schulz-Flory distribution, and the existence of mature potential source rocks have been used to suggest that a thermogenic component exists in the Chimaera gas (Etiope et al., 2011), and it could be argued *a priori* that the $\Delta^{12}\text{CH}_2\text{D}_2$ and $\Delta^{13}\text{CH}_3\text{D}$ -derived temperatures are compromised by this mixing. We can test this hypothesis with the resolved $\Delta^{12}\text{CH}_2\text{D}_2$ and $\Delta^{13}\text{CH}_3\text{D}$ measurements. For this purpose we first assume “typical” δD and $\delta^{13}\text{C}$ values for the thermogenic and abiotic endmembers with formation temperatures of $\sim 160\text{ }^\circ\text{C}$ and $\sim 35\text{ }^\circ\text{C}$, respectively, represented by thin solid lines in Figs. 13 and 14. If both gases are in bond-order equilibrium at the time of their formation (a disequilibrium isotopic bond order case is also shown in Fig. 14), the mixing curve is just slightly below the equilibrium curve in $\Delta^{12}\text{CH}_2\text{D}_2$ vs. $\Delta^{13}\text{CH}_3\text{D}$ space (Fig. 14); clear deviations from the equilibrium curve due to mixing would not be expected in this case because the difference in δD between the gases is not large enough (Fig. 13). However, if the isotope bond ordering in the Chimaera CH_4 were indeed due to mixing between a low-temperature abiotic component and a thermogenic component, the gas would have to be dominantly thermogenic ($>80\%$) based on the high temperature recorded by

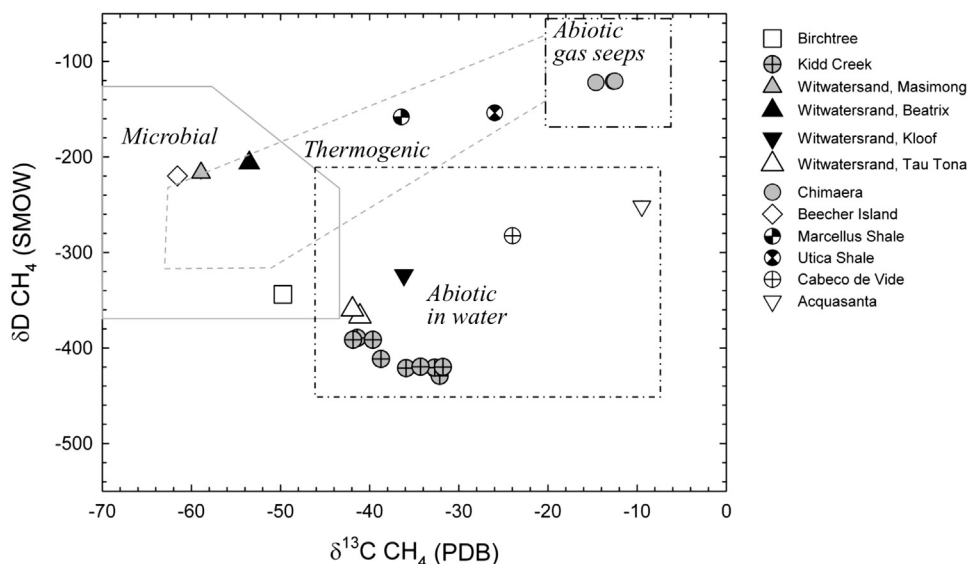


Fig. 11. δD (VSMOW) and $\delta^{13}\text{C}$ (VPDB) of gases used in this study. Nominal fields for microbial, thermogenic and abiotic gas based are also shown for reference and are based on previously published literature compilations (e.g., Etiope and Sherwood Lollar, 2013, and references therein). Abiotic gases are further divided into two fields, those gases dissolved in waters and those issuing from gas seeps.

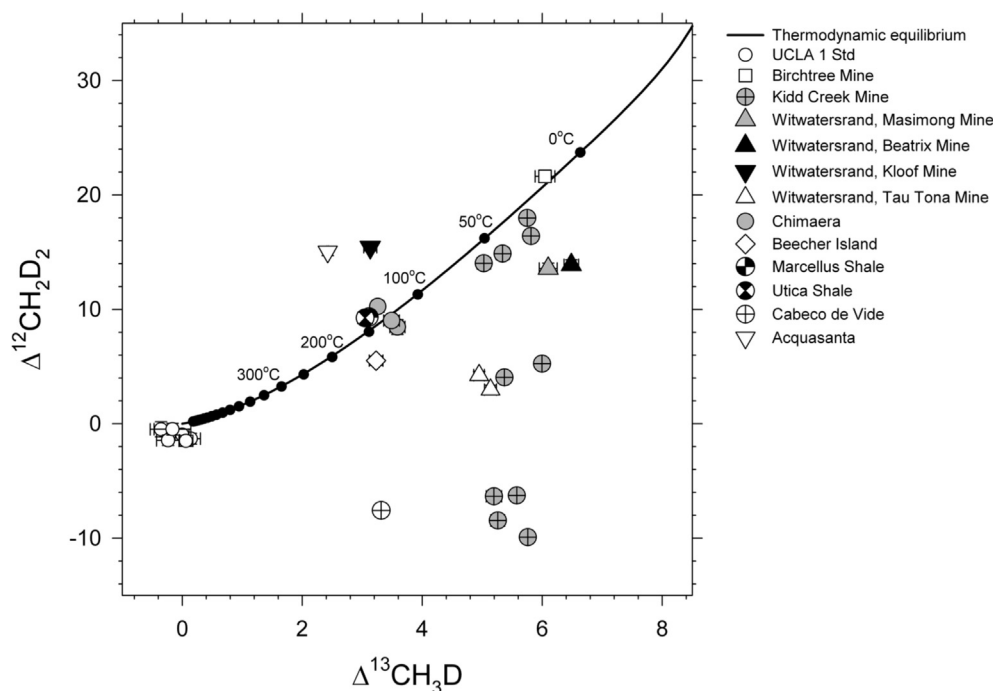


Fig. 12. $\Delta^{12}\text{CH}_2\text{D}_2$ vs $\Delta^{13}\text{CH}_3\text{D}$ for all natural samples in this study. The curve denoting thermodynamic equilibrium is shown for reference. Also shown are replicates of an in-house standard, UCLA-1, as an illustration of external precision.

the relative abundances of both mass-18 isotopologues (Fig. 14). This conclusion is not sensitive to the exact temperatures involved. As an illustration, we consider several possible mixing scenarios in Fig. 15. Three distinct mixing curves are shown in Fig. 15, each marked with white circles showing 10% increments of mixing. Matching the measured Chimaera values by mixing of abiotic gas formed at 80 °C with a higher-temperature thermogenic component formed at ~180 °C would still require that the thermogenic component comprises 70–80% of the Chimaera gas (Fig. 15). Previous work has suggested only 10–20% for the mixing ratio of the thermogenic component. Of course, mixing between gases formed at similar temperatures (within 20° of one another) and with relatively similar δD values cannot be ruled out in any mixing ratio. Nonetheless, the temperature of the abiotic component is constrained by the plausible amounts of thermogenic gas in the mixture. Mixing between a 120 °C abiotic gas with a 180 °C thermogenic gas would suggest that Chimaera CH_4 consists of at least ~40% thermogenic gas (Fig. 15). The mixing ratio of thermogenic gas required by the data decreases as the inferred temperature of the abiotic component increases. In all cases where the thermogenic methane is thought to be the subordinate component, as suggested by the bulk isotope ratios of the Chimaera methane, the $\Delta^{12}\text{CH}_2\text{D}_2$ and $\Delta^{13}\text{CH}_3\text{D}$ data require that the abiotic component formed or equilibrated at high temperatures of $>>120$ °C and ≤ 140 °C (allowing for a sizable but still subordinate thermogenic component for the lower limit and the uncertainty in the calculated equilibrium temperature for the upper limit), or that the gas is in the main thermogenic. Since the bulk isotope ratios of the Chimaera methane would be unusual for a thermogenic gas (higher in $\delta^{13}\text{C}$

and δD), the $\Delta^{12}\text{CH}_2\text{D}_2$ and $\Delta^{13}\text{CH}_3\text{D}$ values are best interpreted as being dominated by an abiotic gas component formed at 120–140 °C.

This temperature range from the $\Delta^{13}\text{CH}_3\text{D}$ and $\Delta^{12}\text{CH}_2\text{D}_2$ data is higher than estimates for ambient temperatures at depth today. The modern geothermal gradient suggests that the current maximum temperatures in the ophiolite nappe, where methane is thought to originate, is ~80 °C (Etiopie et al., 2011). Because the Chimaera sampling site is far removed from known hydrothermal systems in an area of comparatively low heat flow for the region (Ilkisik, 1995; Aydin et al., 2005), intra-species temperatures of 120–140 °C suggest CH_4 formed during a different era where temperatures were higher, perhaps resulting from the exothermic properties of the serpentinization itself (Schuiling, 1964; Allen and Seyfried, 2004) or during emplacement of the ophiolite near the high-temperature metamorphic sole (shear zone) (Etiopie et al., 2016). The continuous exposure of the gas to ultramafic rock surfaces with their potentially catalytic properties may be one factor contributing to its eventual intra-species equilibration.

The conclusion from the Chimaera methane mass-18 isotopologue data is that the major component of the methane gas effusing at this site is abiotic and formed at about 120–140 °C. We also conclude from these data that $\text{CH}_4\text{-H}_2$ D/H thermometry yields spurious temperatures due to inter-species disequilibrium.

5.3. Marcellus and Utica shales

Methane gases from the Marcellus and Utica shales also possess equilibrium distributions of the mass-18 isotopologues and therefore reliable temperatures of formation or

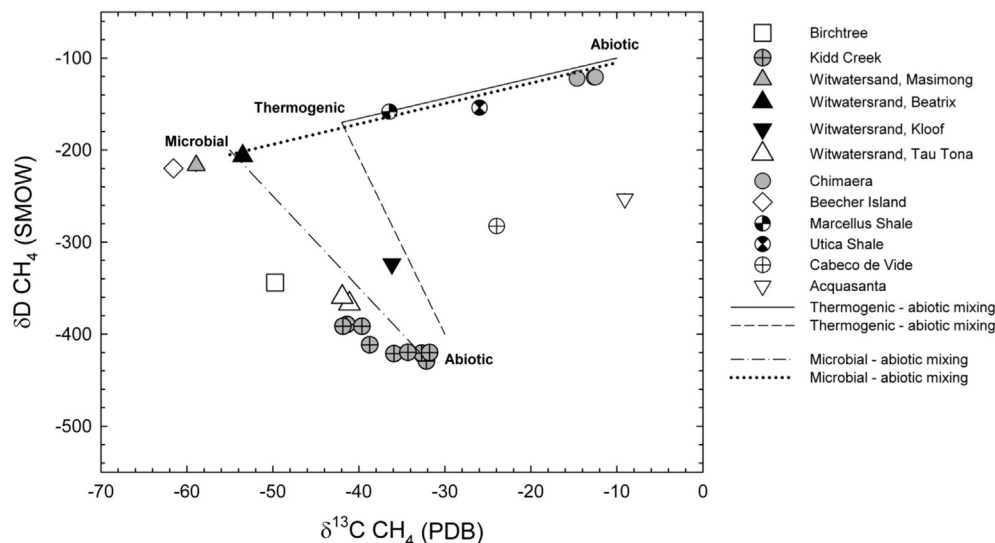


Fig. 13. Mixing scenarios discussed in the text in δD (SMOW) vs. $\delta^{13}C$ (PDB) space.

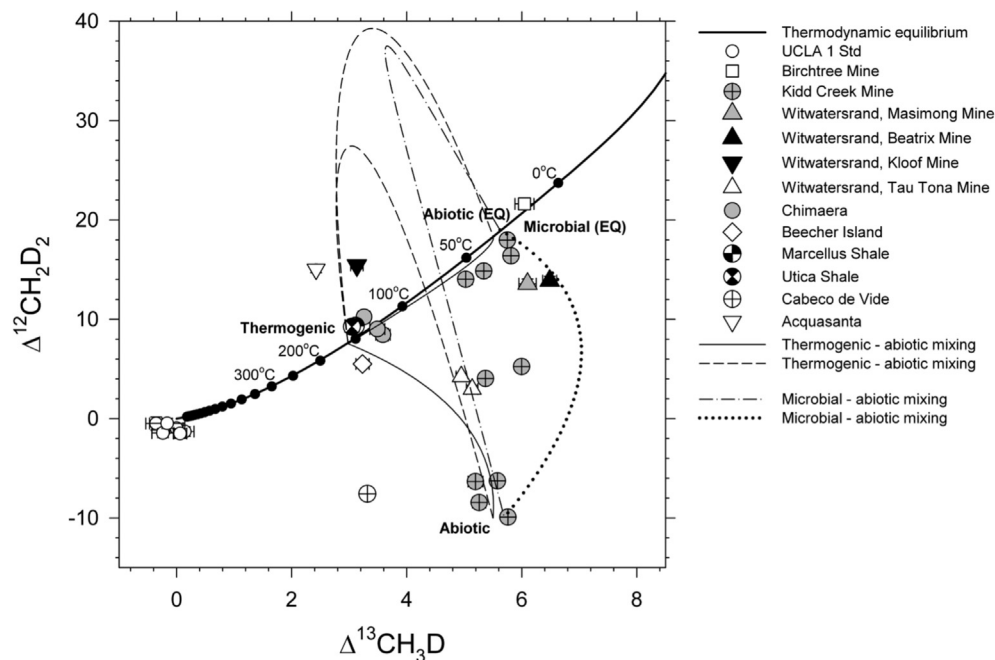


Fig. 14. Mixing scenarios discussed in the text in $\Delta^{12}CH_2D_2$ vs. $\Delta^{13}CH_3D$ space. Some of the endmember compositions discussed in the text are labeled. Abiotic (EQ) and Microbial (EQ) refer to methane gases produced by abiotic reactions or by microbial activity that have equilibrium isotope bond ordering. Two dashed curves depicting mixing between a thermogenic component on the equilibrium curve and two different abiotic endmember compositions, one in thermodynamic equilibrium and the other not, are shown. The compositions of the endmembers are indicated by the terminal points on each curve.

equilibration are obtained (Fig. 12). We calculate an equilibrium temperature of $145^\circ C + 6/-6$ using the data in Table 1 (1 se for the single analysis and using the more precise $\Delta^{13}CH_3D$ value). Our result for the Marcellus gas agrees with the $147^\circ C + 25/-22$ found by Wang et al. (2015) using $\Delta^{13}CH_3D$ alone as measured by tunable laser spectroscopy. Our temperature is lower than the $179-207^\circ C$ found by Stolper et al. (2014a) using unresolved Δ

($^{13}CH_3D + ^{12}CH_2D_2$) and it is also lower than the thermal model for methane generation described by these authors (see above). Results reported here suggest that methane did not form, or last equilibrate, at peak burial temperatures if thermal models cited above are correct. We obtain a temperature of $155^\circ C + 10/-9$ for the Utica Shale gas, suggesting a slightly higher temperature for the gas from this stratigraphically deeper reservoir (Fig. 12). In this

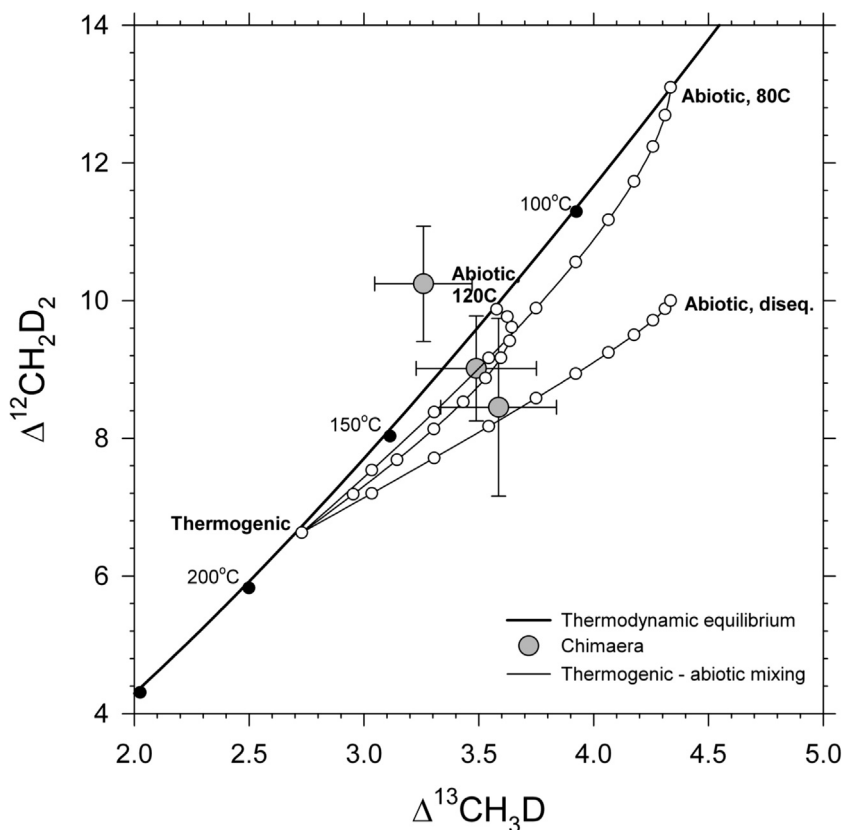


Fig. 15. Mixing scenarios discussed in the text in $\Delta^{12}\text{CH}_2\text{D}_2$ vs. $\Delta^{13}\text{CH}_3\text{D}$ space specific to the Chimaera CH_4 gas. Various possible abiotic endmember compositions are shown, including equilibrated gases at 80 °C and 120 °C and a disequilibrium component, mixed with a thermogenic gas formed at 180 °C. The thin solid lines correspond to the mixing path in δD vs $\delta^{13}\text{C}$ space shown with the same line solid line symbol in Fig. 13. White circles mark 10% intervals of mixing ratios for each of the three mixing curves. The error bars for the Chimaera data represent 2 se (internal errors) in this Figure. The thermodynamic equilibrium curve is shown as the heavy line with black dots for reference.

instance the temperature of formation of the shale-derived methane, fortified by the fact that both mass-18 isotopologues are consistent with thermodynamic equilibrium, requires revision of the temperature of methane formation in the source rocks.

5.4. Birchtree Mine

The methane from the Birchtree Mine yields an equilibrium (i.e., concordant) temperature of $16\text{ °C} + 6/-4$ (Fig. 12). This temperature is similar to the 20–23 °C water temperature in the mine. The bulk isotopic composition of this gas is consistent with microbial methanogenesis. The low temperature similar to the current water temperature is further indication that this gas is affected by extant biological processing in the environs of these waters at shallow depths. This conclusion is bolstered by the presence of active methanogens in the Thompson mine on the same property. The fact that CH_4 from the Birchtree mine is in intra-species isotopic bond order equilibrium, has bulk isotope ratios suggestive of a significant microbial component, and formed at temperatures consistent with the present-day water temperatures, all suggest that microbial processing in natural settings can lead to equilibrium isotopic bond ordering.

5.5. Natural samples exhibiting disequilibrium

The CH_4 samples described in Sections 5.6 through 5.8 exhibit different degrees of isotopic bond order disequilibrium. The gases with the greatest degrees of disequilibrium, including those sampled at Kidd Creek, Tau Tona, and Cabeco de Vide, have $\Delta^{12}\text{CH}_2\text{D}_2$ and $\Delta^{13}\text{CH}_3\text{D}$ characteristics resembling those of methane produced by abiotic synthesis in the laboratory (Section 4.2). The Masimong and Beatrix samples have smaller but still substantial negative excursions in $\Delta^{12}\text{CH}_2\text{D}_2$ relative to equilibrium. The Beecher Island gas shows a small but important departure from equilibrium. Kloof and Acguasanta Terme samples display apparent excesses in $^{12}\text{CH}_2\text{D}_2$ rather than deficits that suggest a process of isotope fractionation or perhaps mixing. In all of these cases, temperatures of formation cannot be obtained quantitatively. However, comparisons with our experimental data and consideration of the geological context for each sample lead to new insights into the provenance of methane at each site.

5.6. Beecher Island

The Beecher Island gas field sample exhibits a small but resolvable depletion in $^{12}\text{CH}_2\text{D}_2$ relative to equilibrium that

signifies disequilibrium (Fig. 12). This depletion casts doubt on the veracity of temperatures derived from isotope clumping. The small but resolvable disequilibrium is a valuable example of how a temperature deduced from $\Delta^{13}\text{CH}_3\text{D}$ alone, that otherwise appears perfectly reasonable, may in fact be spurious and therefore misleading. The Beecher Island bulk δD and $\delta^{13}\text{C}$ values are well within the ranges expected for a microbial gas but also overlap values for some thermogenic gases (Fig. 11). However, at face value the temperature from $\Delta^{13}\text{CH}_3\text{D}$ is $142\text{ }^\circ\text{C}\pm 8$ while the practical upper temperature limit for microbial processing of methane is $\sim 80\text{ }^\circ\text{C}$ (Valentine, 2011), growth of methanogens in the laboratory at higher temperatures of $122\text{ }^\circ\text{C}$ not withstanding (Takai et al., 2008). The $\Delta^{13}\text{CH}_3\text{D}$ temperature value is therefore clearly higher than expected for a “biogenic” (meaning microbial in this context) gas, but this disagreement alone is not sufficient evidence to reject the clumping temperature. Rather, the lack of mass-18 isotopologue equilibrium (i.e., concordant temperatures) is evidence that the temperature obtained from clumped isotopes should be considered unreliable, and that further study is required. For example, the face-value $\Delta^{13}\text{CH}_3\text{D}$ temperature of $\sim 140\text{ }^\circ\text{C}$ could suggest that the Beecher Island gas is not “biogenic” (i.e., microbial) but rather thermogenic, and therefore similar to gases from deeper in the Niobrara Formation. However, the presence of disequilibrium concentrations of the rare isotopologues cast doubt on this conclusion. The ability to identify isotopologue disequilibrium even where the temperature derived from $\Delta^{13}\text{CH}_3\text{D}$ alone is plausible is a considerable benefit afforded by these data. Departures from equilibrium in both mass-18 methane isotopologues as a consequence of microbial activity are consistent with our observations of methanogenesis in the laboratory (Fig. 8). Spuriously high $\Delta^{13}\text{CH}_3\text{D}$ temperatures due to isotopic bond order disequilibrium are also consistent with previous reports (Wang et al., 2015).

5.7. Kidd Creek, Tau Tona, and Cabeço de Vide

Dramatic departures from equilibrium are found in methane effusing from relatively cool waters from the deep mines and from the Cabeço de Vide spring. Three distinct localities, including Kidd Creek, Tau Tona, as well as Cabeço de Vide, representing two distinct Precambrian shields and an unrelated ultramafic complex, all exhibit large depletions in $\Delta^{12}\text{CH}_2\text{D}_2$ of up to $\sim 25\%$ relative to equilibrium (Fig. 12). Two additional Witwatersrand mine samples, from Masimong and Beatrix, also show substantial negative excursions in $\Delta^{12}\text{CH}_2\text{D}_2$ relative to equilibrium (Fig. 12). The bulk isotopic compositions of these disequilibrium samples are all very different from one another (Fig. 11).

The most extensively sampled of these is the Kidd Creek mine. Water temperatures in the mine are $\sim 20\text{ }^\circ\text{C}$ to $30\text{ }^\circ\text{C}$, and the $\Delta^{13}\text{CH}_3\text{D}$ values for all of the Kidd Creek samples, from both the 7850 and 9500 foot levels and collected over a period of 8 years, are broadly consistent with this temperature, although with many measurements scattered to somewhat higher apparent temperatures near $50\text{ }^\circ\text{C}$. The

$\Delta^{12}\text{CH}_2\text{D}_2$ is highly variable from -10% to near equilibrium (Fig. 12). The most $^{12}\text{CH}_2\text{D}_2$ depleted samples come from the deeper 9500 foot level of the mine (Table 1). However, because the samples represent a time interval of nearly 8 years, we are able to identify a time-dependence to the $\Delta^{12}\text{CH}_2\text{D}_2$ values that suggests that the disparate $\Delta^{12}\text{CH}_2\text{D}_2$ values are not a function of level in the mine but rather depend on the time of exposure to the outside world. Sherwood Lollar et al. (2002) reported the presence of abiotic-dominated CH_4 from the 6800 foot level. The $\delta^{13}\text{C}$ CH_4 and $\text{C1/C2} +$ values for the 6800 samples overlap those of the 9500 foot level. Both sets of samples were collected within months of borehole completion. In contrast, the samples from the 7850 boreholes were sampled 5 years after completion and exhibit lower $\delta^{13}\text{C}$ values (Table 1) and higher $\text{C1/C2} +$. Indeed, all of the methane isotope ratios are varying with time at Kidd Creek. For example, Fig. 16 shows covariation of δD , $\delta^{13}\text{C}$, and $\Delta^{12}\text{CH}_2\text{D}_2$ with days since the borehole was drilled.

The question arises as to the commonality between the deep mine methane and the methane degassing from the spring at Cabeço de Vide that results in low $\Delta^{12}\text{CH}_2\text{D}_2$ values. It seems likely that the link is surface catalysis followed by preservation by entrainment in water at relatively low temperatures. Like the abiotic gases from the Precambrian shields, the Cabeço de Vide methane is likely to have been produced by FTT reactions. And, like the deep mine gases, this gas was entrained in cool water. In each of these settings, it is possible that the signature low $\Delta^{12}\text{CH}_2\text{D}_2$ values are preserved by the relatively low temperatures at which the CH_4 gases reside. While the $\Delta^{13}\text{CH}_3\text{D}$ values of the Kidd Creek methane samples are crudely consistent with the inferred low-temperatures of formation, we demonstrated with experiments (Section 4.2) that where $\Delta^{12}\text{CH}_2\text{D}_2$ is greatly depleted, $\Delta^{13}\text{CH}_3\text{D}$ can also be in part kinetically controlled in general (e.g., the $70\text{ }^\circ\text{C}$ Sabatier reaction, Fig. 7). Therefore, we do not think that the apparent $\Delta^{13}\text{CH}_3\text{D}$ temperature of $\sim 150\text{ }^\circ\text{C}$ for the Cabeço de Vide sample can be taken as reliable evidence that the gas was formed at such high temperatures. Nonetheless, more work should be undertaken at this site because the similarity between the equilibrium temperature obtained from the Chimaera samples and the Cabeço de Vide sample is intriguing.

5.8. Masimong and Beatrix

The Masimong and Beatrix gases are believed to be largely microbial in origin at present (Section 3.1), and among the deep mine gases, they exhibit the closest approaches to equilibrium (superseded only by the Birchtree sample that is entirely equilibrated and also dominated by microbial methanogenesis). This observation, in combination with the time variability towards equilibrium over several years documented at Kidd Creek, suggests that in all of the deep mines, methane was produced abiotically with telltale low $\Delta^{12}\text{CH}_2\text{D}_2$ values caused by tunneling that are progressively erased by the incursion of biological activity that drives the isotopic bond ordering in methane towards equilibrium. The data imply that the microbial communities

influence methane isotopic values once the boreholes are drilled.

At Beatrix, Tau Tona and Masimong archaea are estimated to comprise ~1.5% (Simkus et al., 2016), ~4% (Simkus et al., 2016), and 11% (this study), respectively, of the sampled (planktonic) microbial communities. These archaeal communities are dominated by methanogens within the Methanobacteria, Methanomicrobia, and methanogen-containing Thermoplasmata classes. Anaerobic methane oxidizers within the ANME-1, ANME-2 and ANME-3 clades are also present. PLFA (Simkus et al., 2016), molecular (DNA, RNA, protein), and enrichment experiments (Magnabosca et al., 2016) have provided further evidence for anaerobic methane oxidation in these deep mine environs. Therefore, the deep mines likely exhibit active methane cycles in which methanogens produce methane and the ANME groups destroy methane by anaerobic methane oxidation.

5.9. Thermometry pitfalls

The broad agreement between $\Delta^{13}\text{CH}_3\text{D}$ values and host water temperatures for the deep mine methane gases exhibiting pronounced D–D bond order disequilibrium is at once a useful property and a seductive pitfall. This relationship might prove useful as a general indicator of formation temperature but might also be mistakenly used to infer that $\Delta^{13}\text{CH}_3\text{D}$ is always a robust temperature indicator regardless of evidence for disequilibrium. The progression of CH_4 isotopologue ratios with time at Kidd Creek is essentially vertical in $\Delta^{12}\text{CH}_2\text{D}_2$ vs. $\Delta^{13}\text{CH}_3\text{D}$ space and trends toward equilibrium temperatures of ~30 to 50 °C, within $\leq 20^\circ$ of the present-day water temperatures of ~23 °C to 33 °C (Fig. 12). The $\Delta^{13}\text{CH}_3\text{D}$ data for the Masimong, Beatrix, and Tau Tona mines are also crudely consistent with the water temperatures of ~30 °C. This rough agreement between host water temperatures and temperatures derived from ^{13}C -D isotope clumping despite clear evidence for D–D isotopic bond order disequilibrium is similar to the pattern obtained in the Sabatier reactions in the

laboratory: differences in H and D tunneling impart larger kinetic effects for $^{12}\text{CH}_2\text{D}_2$ than for $^{13}\text{CH}_3\text{D}$. The agreement between expected temperatures and $\Delta^{13}\text{CH}_3\text{D}$ temperatures in these instances is in part fortuitous, however. Relatively large variations in $\Delta^{13}\text{CH}_3\text{D}$ of nearly 1‰ correspond to shifts of only ~20° in the vicinity of 30 °C (Fig. 12). At these temperatures, relatively sizable kinetic effects in $\Delta^{13}\text{CH}_3\text{D}$ values have muted impacts on calculated temperatures. For comparison, consider that a kinetically-induced 1‰ spread in $\Delta^{13}\text{CH}_3\text{D}$ values at temperatures >100 °C corresponds to temperature differences of $\geq 100^\circ$. Therefore, because of the low temperatures involved, the $\Delta^{13}\text{CH}_3\text{D}$ values for these samples might be taken as supporting evidence for low temperatures of formation in general as deduced by other means but should not be used as quantitative thermometers.

For example, the assumption of liquid H_2O – H_2 D/H isotope exchange equilibrium yields relatively low temperatures of 30–33 °C for the 7850 Kidd Creek samples and 44–56 °C for the 9500 Kidd Creek samples (Table 1). These compare reasonably well with the ~20 °C and ~30 °C water temperatures at 7850 and 9500 foot levels in the mine, respectively, especially in view of the >20° scatter observed where this thermometer has been applied at other localities (e.g., Proskurowski et al., 2006). The origin of H_2 gas in these geological settings by water–rock reactions or by radiolysis argues for an approach to isotopic equilibrium between water and H_2 gas. The hydrogen isotope data for waters and H_2 gases are generally consistent with D/H equilibrium. On the other hand, CH_4 and H_2 D/H partitioning does not agree with these other two temperature indicators, yielding apparent temperatures of 84–172 °C (Table 1). Comparison of the $\Delta^{12}\text{CH}_2\text{D}_2$ vs. $\Delta^{13}\text{CH}_3\text{D}$ systematics of the abiotic methane production experiments with the $\Delta^{12}\text{CH}_2\text{D}_2$ vs. $\Delta^{13}\text{CH}_3\text{D}$ data from the deep mines, together with the inter-species thermometry results, suggests that the best interpretation is that methane gases from the Canadian shield and Witwatersrand Basin deep mines formed at temperatures $\leq 50^\circ\text{C}$ and that these gases are not in D/H equilibrium with their host waters or with the coexisting

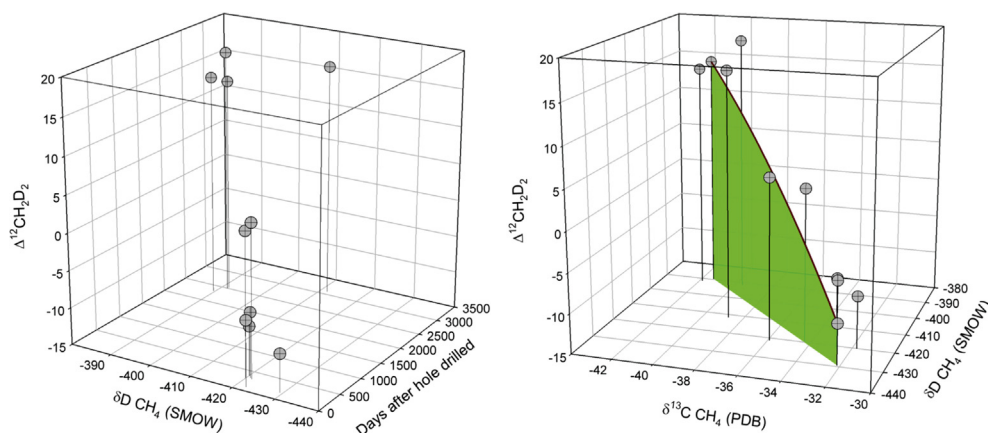


Fig. 16. Plots of methane δD and $\Delta^{12}\text{CH}_2\text{D}_2$ vs. days since borehole at Kidd Creek was drilled (left) and δD , $\Delta^{12}\text{CH}_2\text{D}_2$ and $\delta^{13}\text{C}$ for the same samples. The curve on the right-hand panel is a mixing model between the two extreme compositions. The shaded panel is to enhance the perspective view for the mixing curve.

H₂ gas. Sherwood Lollar et al. (2008) arrived at similar conclusions based on the inter-species D/H partitioning and the kinetics of inter-species D/H exchange.

Deuterium-hydrogen isotope exchange disequilibrium between CH₄ and H₂ like that proposed for the deep mine gases was also proposed above for the Chimaera gases based on disagreement between the concordant, equilibrium $\Delta^{12}\text{CH}_2\text{D}_2$ vs. $\Delta^{13}\text{CH}_3\text{D}$ temperatures and the CH₄-H₂ exchange equilibrium temperatures at that site (Table 1). The prevalence of inter-species disequilibrium suggests that D/H exchange is not a reliable thermometer for CH₄ formation. We note that the e-fold timescale for hydrogen isotope exchange equilibration between water and methane is ~ 1 Myr at 200 °C (Sessions et al., 2004), suggesting that at temperatures of <100 °C equilibration timescales may be on the order of ~ 10 Myr. None of the samples for which we have δD values for both H₂O and coexisting CH₄ are in hydrogen isotopic equilibrium at the measured water temperatures (Table 1). The inter-phase isotopic disequilibrium suggests that the CH₄ gas has been in persistent contact with its host water for timescales of less than tens of millions of years. Sequestration in relatively cool waters for timescales of less than 10^7 y explains the preservation of disequilibrium isotopic bond ordering in all but one of the aqueous CH₄ samples (the exception being the Birchtree gas that is evidently largely if not entirely microbial in origin).

5.10. Abiotic – biotic gas mixing

In earlier studies (Sherwood Lollar et al., 2007) it was proposed that a trend in δD vs $\delta^{13}\text{C}$ space between nominally abiotic methane gas resembling Kidd Creek and microbial gas resembling methane sampled at Masimong and Beatrix represents mixing between typical microbial (“M”) and abiotic (“A”) gases. We can use $\Delta^{13}\text{CH}_3\text{D}$ and $\Delta^{12}\text{CH}_2\text{D}_2$ to test this mixing scenario. The microbial-abiotic mixing proposed previously is shown in Fig. 13 with the dash-dot-dash line. This mixing is shown in mass-18 isotopologue space in Fig. 14 with the same line symbol. In this case we use the maximum deficit in $\Delta^{12}\text{CH}_2\text{D}_2$ exhibited by the samples from Kidd Creek for the abiotic end-member and a microbial end-member that is assumed to be equilibrated at 30 °C (representing gas equilibrated at present-day water temperatures). The point at which the mixing curve crosses the equilibrium curve in Fig. 14 corresponds to a mixing ratio for the microbial component of 14%. For larger proportions of microbial gas, the large differences in δD between Kidd-Creek-like abiotic gas and microbial gas would result in large positive $\Delta^{12}\text{CH}_2\text{D}_2$ excursions from the equilibrium curve upon mixing. Since the gases from Masimong and Beatrix mines lie below the equilibrium curve, rather than above it, and yet exhibit bulk isotopic ratios suggesting large microbial components, we find that the mass-18 isotopologue data are not consistent with this mixing scenario. Mixing between this same microbial end-member used above and an abiotic component similar to the Chimaera gas in δD and $\delta^{13}\text{C}$ is also shown in Figs. 13 and 14 with dotted lines. In this case the differences in δD are smaller, and so the mixing curve never crosses the equilibrium curve in Fig. 14. Although the dotted curve in

Fig. 14 more closely resembles the deep mine gases in $\Delta^{13}\text{CH}_3\text{D}$ and $\Delta^{12}\text{CH}_2\text{D}_2$, there is no evidence for a methane component resembling the Chimaera gas in the deep mine systems (Fig. 13).

The failure of the “M” – “A” mixing model does not mean that the Kidd Creek gases with intermediate $\Delta^{12}\text{CH}_2\text{D}_2$ values are not the result of mixing between the gases with the lowest $\Delta^{12}\text{CH}_2\text{D}_2$ values and those with the highest, near-equilibrium values. All of the methane isotope data at Kidd Creek can be explained reasonably well by mixing between the two most extreme samples. The right-hand panel of Fig. 16 shows a mixing curve through the data illustrating this point (this same curve is essentially vertical through the data in Fig. 14). By extension, we suggest that the gases from Tau Tona may also be mixtures between abiotic gas with very low $\Delta^{12}\text{CH}_2\text{D}_2$ values and gases driven closer to equilibrium by microbial activity. Likewise, the low $\Delta^{12}\text{CH}_2\text{D}_2$ values of the Beatrix and Masimong gases may also be vestiges of the abiotic component, although disequilibrium resulting from microbial processing cannot be ruled out.

5.11. Kloof and Acguasanta Terme apparent excesses in $^{12}\text{CH}_2\text{D}_2$

Two methane samples lie above the equilibrium curve in Fig. 12 rather than below it. These are the Witwatersrand Kloof Mine sample and the sample from the Acguasanta Terme hyperalkaline spring. In both cases it is clear that a temperature obtained from $\Delta^{13}\text{CH}_3\text{D}$ would be incorrect. In general, positive $\Delta^{12}\text{CH}_2\text{D}_2$ displacements from the equilibrium curve can be attributable to either mixing of gases with disparate δD values or fractionation of the bulk isotopic composition of the gas without bond re-ordering (i.e., without bond rupture and reformation), as described above (Fig. 3). We show in Figs. 13 and 14 a mixing scenario that attempts to explain the isotopic composition of the Kloof mine methane, for example. In this model equilibrated thermogenic gas, seemingly required by the relatively low $\Delta^{13}\text{CH}_3\text{D}$ values for the Kloof gas, is mixed with an abiotic component to explain the relatively low δD values (Fig. 13). Two different abiotic methane components are considered, one with very low $\Delta^{12}\text{CH}_2\text{D}_2$ values resembling the more primitive Kidd Creek gases, and the other equilibrated at 30 °C, resembling the Kidd Creek gases driven towards isotope bond ordering equilibrium by microbial processing (Fig. 14). The results are shown as dashed lines in both Figs. 13 and 14. While not meant to be a quantitative fit to the data, one can see that positive excursions in $\Delta^{12}\text{CH}_2\text{D}_2$ relative to equilibrium can be produced by such a scenario. A thermogenic component derived from breakdown of organics in the Witwatersrand Supergroup has been proposed in the past, but there is nothing in the geological setting of the Kloof Mine that constitutes compelling evidence for a thermogenic source. Similar circumstances obtain for the Acguasanta gas; there is no compelling evidence for a thermogenic component but one cannot be ruled out either.

An alternative explanation for the disequilibrium $\Delta^{12}\text{CH}_2\text{D}_2$ and $\Delta^{13}\text{CH}_3\text{D}$ values for these gases is that they

were affected by a kinetic process that raised their bulk δD and $\delta^{13}C$ values, thus altering the stochastic reference frame for calculating the $\Delta^{12}CH_2D_2$ and $\Delta^{13}CH_3D$ values. In this case the distribution of rare isotopologues is no longer consistent with the bulk isotopic composition, resulting in spuriously high $\Delta^{12}CH_2D_2$ values relative to $\Delta^{13}CH_3D$ values. A simple but unlikely candidate is molecular diffusion (e.g., Fig. 3). The latter is simple to model and serves as an illustration of the effect. We show such a model in Fig. 17. In this case the initial gas is chosen to be equilibrated at 30 °C and to have a bulk isotopic composition resembling the Birchtree gas. The model curves in Fig. 17 show the evolution of the residual gas following Rayleigh distillation by molecular diffusion. While the calculation could explain both the Kloof and the Acquisanta gases in clumping space, the trend in bulk isotope ratio space is shallower than the trend defined by these data taken together. However, there is no reason to assume that the starting compositions for the two methane sites were the same. Therefore, it remains true that a process that fractionates the methane according to molecular weight could explain the positive $\Delta^{12}CH_2D_2$ deviations from the equilibrium curve as well as apparent increases in $\delta^{13}C$ with only modest increases in δD relative to other deep mine gases. A search for candidate processes would seem warranted. In all cases, the essential point is that clumped isotopes of these gases do not yield temperatures.

6. DISCUSSION

The telltale signature of catalyzed abiotic methane formation caused by the different tunneling behaviors of protium and deuterium is evidently preserved where methane is sequestered in ground waters (e.g., the deep mine gases and the Cabeco de Vide spring). This abiotic signature may never form at higher temperatures in some natural settings or may be erased with prolonged and direct exposure of CH_4 gas to rock surfaces (e.g., Chimaera). This relatively simple picture is modified substantially by microbial pro-

duction and/or cycling of methane gas. The consequences of spatially-overlapping abiotic methane migration and microbial methane production and cycling is discussed below.

6.1. Biological processing of CH_4

Results of several studies of clumped isotopes in methane show that equilibrium in $\Delta^{13}CH_3D$ can occur with biological production of methane gas (Stolper et al., 2015; Wang et al., 2015). The factors governing the degree of isotope bond order equilibrium or disequilibrium in microbial CH_4 production are at present unclear, in part because the kinetic pathways are still matters of active investigation (Wongnate et al., 2016). Wang et al. (2015) used a Michaelis–Menton formulation for the kinetics of microbial methane production that highlights the potential reversibility of the enzymatic process. They linked the degree of reversibility to the availability of H_2 . The concept of reversibility is consistent with the reversibility of archaeal methanogenesis and anaerobic oxidation of methane (AOM) afforded by the methyl-coenzyme M reductase (MCR) common to organisms responsible for these two processes (Scheller et al., 2010), and enzymatically-driven $^{13}C/^{12}C$ equilibration in CH_4 by AOM has been reported previously (Ysohinaga et al., 2014). An open question is whether isotopic bond order equilibration can occur with only minor effects on bulk δD and $\delta^{13}C$ values by microbial processing of a reservoir of CH_4 . Continuous production (archaeal methanogenesis) simultaneous with destruction (e.g., AOM) of CH_4 by the opposing effects of similar enzymatic activities operating in reverse directions (i.e., production of CH_4 favoring light isotopes in concert with binding and destruction of CH_4 that also favors the lighter isotopes) may result in a near steady state in terms of bulk isotopic composition that resembles the original source of methane. Methane bonds would be remade by the methanogens in this environment and so could be driven to isotopic bond order equilibrium under the right con-

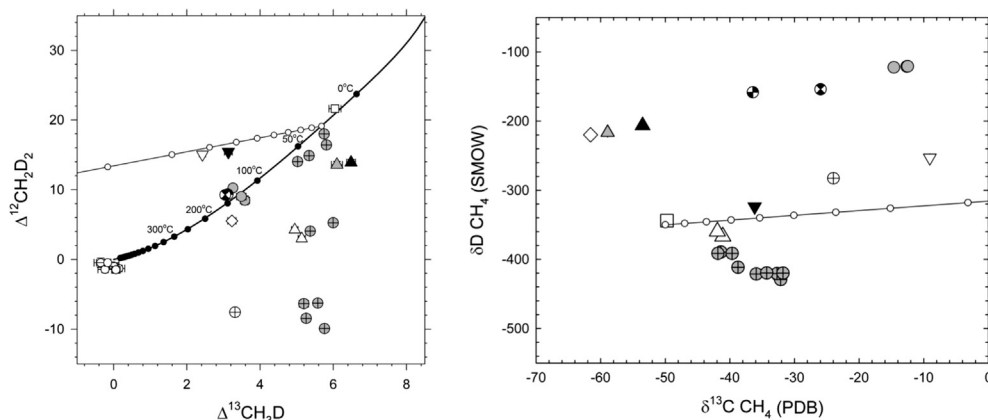


Fig. 17. Plots showing the calculated compositions of methane gas residues following Rayleigh fractionation by molecular diffusion. The residue compositions are shown as the thin solid lines with white small circles in $\Delta^{12}CH_2D_2$ vs. $\Delta^{13}CH_3D$ space (left) and in δD vs. $\delta^{13}C$ space (right). Small white circles are fractions of CH_4 gas remaining in 10% increments, starting with 100%. The initial gas is on the equilibrium curve in $\Delta^{12}CH_2D_2$ vs. $\Delta^{13}CH_3D$ space (thick black curve, left panel) at 30 °C. Sample symbols are the same as in the previous figures.

ditions. The effect of microbial communities on methane isotope clumping is fertile ground for future research. For now, based on the CH_4 isotope data collected from the various sampling sites presented here, and the presence of both methanogens and methanotrophic archaea (ANME) in the systems approaching equilibrium, we conclude that microbial communities can process methane to produce equilibrium or near equilibrium isotopic bond ordering.

6.2. Competition between abiotic and biotic methane production

The picture that emerges from these studies is one in which abiotic methane can be reprocessed by microbial activity in some settings. Abiotic methane production results in significant depletions in $^{12}\text{CH}_2\text{D}_2$ with more modest or even negligible depletions in $^{13}\text{CH}_3\text{D}$ relative to equilibrium both in the laboratory and in natural settings. The isotopologue signatures of catalyzed abiotic methane formation are evidently preserved where the gas is entrained in cool waters (e.g., Precambrian shield mine gases).

Microbial activity can produce large depletions in both $^{12}\text{CH}_2\text{D}_2$ and $^{13}\text{CH}_3\text{D}$ but can also lead to equilibrium $\Delta^{12}\text{CH}_2\text{D}_2$ and $\Delta^{13}\text{CH}_3\text{D}$ values. Methane gases effusing from fracture waters in the deep mines of the Precambrian shields have the significant deficits in $^{12}\text{CH}_2\text{D}_2$ and more modest depletions in $^{13}\text{CH}_3\text{D}$ that we attribute to abiotic methane formation. These pristine gases are subsequently prone to recycling and isotopic bond re-ordering as micro-

bial communities colonize the fractures from which the gases are issuing over time. The equilibrium clumping signature at host water temperatures in the Birchtree mine sample may be an example of this process going to completion. A schematic representing this scenario to explain the deep mine gases is shown in Fig. 18. The figure illustrates the spatial and temporal evolution of the microbial component to the methane gas budget in the rock fracture system as a consequence of opening a new drill hole.

7. CONCLUSIONS

The use of two mass-18 rare isotopologues of methane affords insights into the provenance of methane gases from a variety of natural settings. Where $\Delta^{12}\text{CH}_2\text{D}_2$ and $\Delta^{13}\text{CH}_3\text{D}$ values are inconsistent with thermodynamic equilibrium, temperatures of formation based on one or the other of these species must be considered with suspicion. However, the details of the disequilibrium isotopologue ratios provide important information about the history and even the formation mechanism of the gas. Without measurements of $\Delta^{12}\text{CH}_2\text{D}_2$ to go along with $\Delta^{13}\text{CH}_3\text{D}$ values, spurious but seemingly plausible temperatures obtained with $\Delta^{13}\text{CH}_3\text{D}$ values alone could easily be mistaken for true temperatures of formation. Several examples of this potential pitfall are described in this study.

Where $\Delta^{12}\text{CH}_2\text{D}_2$ and $\Delta^{13}\text{CH}_3\text{D}$ do yield concordant temperatures, representing isotopic bond order equilibrium, we find that these temperatures are sometimes at odds with

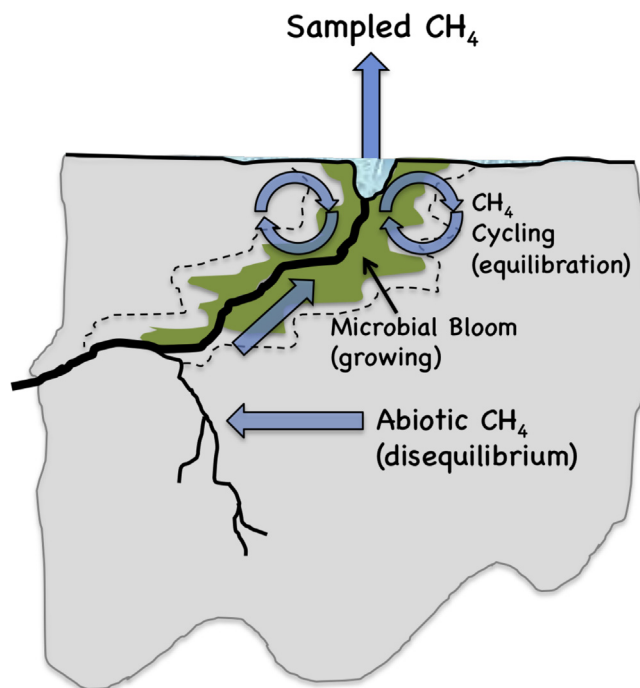


Fig. 18. Schematic illustrating the scenario for abiotic methane production followed by recycling of methane by microbial activity at Kidd Creek and other deep mines. Heavy black lines represent fractures. The green field and the dashed curve represent the extent of current and future microbial communities, respectively. The blue arrows depict the path of methane gas through the fracture system, including cycling by microbial activity near the drill hole (drill hole is shown at the top of the diagram). (For interpretation of the references to colour in this figure legend, the reader is referred to the web version of this article.)

temperatures inferred by indirect means. Equilibrium $\Delta^{12}\text{CH}_2\text{D}_2$ and $\Delta^{13}\text{CH}_3\text{D}$ temperatures that do not match those obtained by D/H exchange thermometry between CH_4 and H_2 and between CH_4 and H_2O suggest that CH_4 is not in D/H exchange equilibrium with either species in the samples studied here, calling into question the general use of inter-species D/H exchange as a reliable thermometer for methane formation except perhaps at higher temperatures than those encountered in this study.

The deficits in $^{12}\text{CH}_2\text{D}_2$ compared with equilibrium values in CH_4 gas made by abiotic reactions are sufficiently large as to point towards a quantum tunneling origin. Tunneling also accounts for the more moderate depletions in $^{13}\text{CH}_3\text{D}$ relative to equilibrium that accompany the low $^{12}\text{CH}_2\text{D}_2$ abundances. This tunneling signature of abiotic methane formation may prove to be an important tracer of abiotic methane formation, especially where it is likely to be preserved by dissolution of gas in cool hydrothermal systems. Eventual applications to methane on Mars are obvious. Mechanisms for erasing the kinetic signature of abiotic methane formation include recycling by biological activity and perhaps prolonged exposure of the gas phase to rock surfaces at temperatures of $\sim 150^\circ\text{C}$ or greater.

The scenario of biological recycling of abiotic methane is a cautionary tale for assigning provenance to CH_4 in general. In the laboratory, methanogenesis produces disequilibrium isotopic bond order effects rivaling those produced by abiotic CH_4 production, although the effects for $^{13}\text{CH}_3\text{D}$ are larger and the effects for $^{12}\text{CH}_2\text{D}_2$ are smaller than in the abiotic gases. In natural settings, however, there is evidence for microbial cycling leading to equilibrium isotopic bond ordering. The conditions leading to isotopic bond order equilibrium in methane produced by, or acted upon by, microbial communities requires further study.

ACKNOWLEDGEMENTS

This research has been supported by the Deep Carbon Observatory (Sloan Foundation), the National Science Foundation's EAR program (0948938 to EDY and DR and 1539023 to EDY), the Department of Energy (DE-SC0006623 to DR and EDY), Shell Projects and Technologies Inc. – Emerging Technologies Group, the ACS Petroleum Research Fund (54848-ND2 to EDY), the Carnegie Institution of Washington (DR), the Natural Sciences and Engineering Research Council of Canada (BSL, CS, OW), the Center for Dark Energy Biosphere Investigations, C-DEBI (IPR, DEL), and the NASA Astrobiology Institute (ARR, DEL). We thank Alvin Ly (UCLA) and Nate Monson (UCLA) for help in the laboratory. We benefited greatly from discussions early on in this project with Weifu Guo (Woods Hole Oceanographic Institution).

REFERENCES

Allen D. E. and Seyfried, Jr., W. E. (2004) Serpentinization and heat generation: constraints from Lost City and Rainbow hydrothermal systems. *Geochem. Cosmochim. Acta* **68**(6), 1347–1354.

Aydin I., Karat H. I. and Kocak A. (2005) Curie-point depth map of Turkey. *Geophys. J. Int.* **162**, 633–640.

Baetzold R. C. and Somorjai G. A. (1976) Preexponential factors in surface reactions. *J. Catal.* **45**, 94–105.

Bell R. P. (1959) The tunnel effect correction for parabolic potential barriers. *Trans. Faraday Soc.* **55**, 1–4.

Bell R. P. (1980) *The Tunnel Effect in Chemistry*. Chapman and Hall, London.

Bigeleisen J. (1955) Statistical mechanics of isotopic systems with small quantum corrections. I. General considerations and the rule of the geometric mean. *J. Chem. Phys.* **23**(12), 2264–2267.

Blamey N. J. F., Parnell J., McMahon S., Mark D. F., Tomkinson T., Lee M., Shivak J., Izawa M. R. M., Banerjee N. R. and Flemming R. L. (2015) Evidence for methane in Martian meteorites. *Nat. Commun.* **6**, 7399.

Borgonie G., Linage-Alvarez B., Ojo A. O., Mundle S. O. C., Freese L. B., Rooyen C. V., Kuloyo O., Albertyn J., Pohl E., Cason E. D., Vermeulen J., Pienaar C., Litthauer D., Van Niekerk H., Van Eeden J., Sherwood Lollar B., Onstott T. C. and Van Heerden A. (2015) Eukaryotic opportunists dominate the deep-subsurface biosphere in South Africa. *Nat. Commun.* **6**, 8952.

Boschetti T., Etiope G. and Toscani L. (2013) Abiotic methane in the hyperalkaline springs of Genova, Italy. *Procedia Earth Planet. Sci.* **7**, 248–251.

Bottinga Y. (1969) Calculated fractionation factors for carbon and hydrogen isotope exchange in the system calcite-carbon dioxide-graphite-methane-hydrogen-water vapor. *Geochem. Cosmochim. Acta* **33**, 49–64.

Brown R. H., Soderblom L. A., Clark R. N., Jaumann R., Barnes J. W., Sotin C., Buratti B., Baines K. H. and Nicholson P. D. (2008) The identification of liquid ethane in Titan's Ontario Lacus. *Nature* **454**, 607–610.

Burruss R. C. and Laughrey C. D. (2010) Carbon and hydrogen isotopic reversals in deep basin gas: evidence for limits to the stability of hydrocarbons. *Org. Geochem.* **41**(12), 1285–1296.

Cluff M. A., Hartstock A., MacRae J. D., Carter K. and Mouser P. J. (2014) Temporal changes in microbial ecology and geochemistry in producer water from hydraulically fractured marcellus shale gas wells. *Environ. Sci. Technol.* **48**, 6508–6517.

Cramer B., Krooss B. M. and Littke R. (1998) Modelling isotope fractionation during primary cracking of natural gas: a reaction kinetic approach. *Chem. Geol.* **149**, 235–250.

Cramer B. (2004) Methane generation from coal during open system pyrolysis investigated by isotope specific, Gaussian distributed reaction kinetics. *Org. Geochem.* **35**, 379–392.

Eiler J. M. and Schauble E. (2004) $^{18}\text{O}^{13}\text{C}^{16}\text{O}$ in Earth's atmosphere. *Geochem. Cosmochim. Acta* **68**(23), 4767–4777.

Eren A. M., Morrison H. G., Lescault P. J., Reveillaud J., Vineis J. H. and Sogin M. L. (2015) Minimum entropy decomposition: unsupervised oligotyping for sensitive partitioning of high-throughput marker gene sequences. *ISME J.* **9**, 968–979.

Etiope G. and Ionescu A. (2015) Low-temperature catalytic CO_2 hydrogenation with geological quantities of ruthenium: a possible abiotic CH_4 source in chromitite-rich serpentinized rocks. *Geofluids* **15**, 438–452.

Etiope G. and Schoell M. (2014) Abiotic gas: atypical, but not rare. *Elements* **10**, 291–296.

Etiope G. and Sherwood Lollar B. (2013) Abiotic methane on Earth. *Rev. Geophys.* **51**, 276–299.

Etiope G., Schoell M. and Hosgormez H. (2011) Abiotic methane flux from the Chimaera seep and Tekirova ophiolites (Turkey): understanding gas exhalation from low temperature serpentinization and implications for Mars. *Earth Planet. Sci. Lett.* **310**, 96–104.

- Etiopio G., Vance S., Christensen L. E., Marques J. M. and Ribeiro da Costa I. (2013) Methane in serpentinized ultramafic rocks in mainland Portugal. *Mar. Pet. Geol.* **45**, 12–16.
- Etiopio G., Vadillo I., Whitticar M. J., Marques J. M., Carreira P. M., Tiago I., Benavente J., Jimenez P. and Urresti B. (2016) Abiotic methane seepage in the Ronda peridotite massif, southern Spain. *Appl. Geochem.* **66**, 101–113.
- Foustoukos D. I. and Mysen B. O. (2013) H/D methane isotopologues dissolved in magmatic fluids: stable hydrogen isotope fractionations in the Earth's interior. *Am. Mineral.* **98**, 946–954.
- Foustoukos D. I. and Seyfried W. E. J. (2004) Hydrocarbons in hydrothermal vent fluids: the role of chromium-bearing catalysts. *Science* **304**, 1002–1005.
- Frantz J. D., Popp R. K. and Hoering T. C. (1992) The compositional limits of fluid immiscibility in the system H₂O-NaCl-CO₂ as determined with the use of synthetic fluid inclusions in conjunction with mass spectrometry. *Chem. Geol.* **98**(3–4), 237–255.
- Fu Q., Sherwood Lollar B., Horita J., Lacrampe-Couloume G. and Seyfried W. E. (2007) Abiotic formation of hydrocarbons under hydrothermal conditions: constraints from chemical and isotope data. *Geochem. Cosmochim. Acta* **71**, 1982–1998.
- Glasby G. P. (2006) Abiogenic origin of hydrocarbons: an historical overview. *Resour. Geol.* **56**, 85–98.
- Haghnegahdar M., Schauble E. A. and Young E. D. (2015) *Constructing an Atmospheric Methane Budget using ¹³CH₃D and CH₂D₂ in Sources and Sinks*. American Geophysical Union, San Francisco, CA, p. 827431.
- Holland G., Sherwood Lollar B., Li L., Lacrampe-Couloume G., Slater G. F. and Ballentine C. J. (2013) Deep fracture fluids isolated in the crust since the Precambrian era. *Nature* **497**, 357–362.
- Horibe Y. and Craig H. (1995) D/H fractionation in the system methane-hydrogen-water. *Geochimica et Cosmochimica Acta* **59**, 5209–5217.
- Horita J. and Berndt M. E. (1999) Abiogenic methane formation and isotopic fractionation under hydrothermal conditions. *Science* **285**, 1055–1057.
- Huse S. M., Dethlefsen L., Huber J. A., Welch D. M., Relman D. A. and Sogin M. L. (2008) Exploring microbial diversity and taxonomy using SSU rRNA hypervariable tag sequencing. *PLoS Genet.* **4**(11), 31000255.
- Ilkisk O. M. (1995) Regional heat flow in western Anatolia using silica temperature estimates from thermal springs. *Tectonophysics* **244**, 175–184.
- Jenden P. D., Drazan D. J. and Kaplan I. R. (1993) Mixing of thermogenic natural gases in Northern Appalachian Basin. *AAPG Bull.* **77**, 980–998.
- Kelley D. S., Karson J. A., Fruh-Green G. L., Yoerger D. R., Shank T. M., Butterfield D. A., Hayes J. M., Shrenk M. O., Olson E. J., Proskurowski G., Jakuba M., Bradley A., Larson B., Ludwig K., Glickson D., Buckman K., Bradley A. S., Brazelton W. J., Roe K., Elend M. J., Delacour A., Bernasconi S. M., Lilley M. D., Baross J. A., Summons R. E. and Sylva S. P. (2005) A serpentinite-hosted ecosystem: the Lost City hydrothermal field. *Science* **307**, 1428–1434.
- Kieft T. L., McCuddy M., Onstott T. C., Davidson M., Lin L.-H., Mislowack B., Pratt L., Boice E., Sherwood Lollar B., Lippmann-Pipke J., Pffiffer S. M., Phelps T. J., Gihring T., Moser D. and Van Heerden A. (2005) Geochemically generated, energy-rich substrates and indigenous microorganisms in deep, ancient groundwater. *Geomicrobiol. J.* **22**, 325–335.
- Klinman J. P. (2003) Dynamic barriers and tunneling. *New views of hydrogen transfer in enzyme reactions, Pure Applied Chemistry* **75**, 601–608.
- Krishtalik L. I. (2000) The mechanism of the proton transfer: an outline. *Biochim. Biophys. Acta* **1458**, 6–27.
- Lehr J. H. and Keeley J. (2016) *Alternative Energy and Shale Gas Encyclopedia*. John Wiley & Sons, Hoboken, New Jersey.
- Limbach H.-H., Lopez J. M. and Kohen A. (2006) Arrhenius curves of hydrogen transfers: tunnel effects, isotope effects and effects of pre-equilibria. *Philos. Trans. Royal Soc. B* **361**, 1399–1415.
- Lin L.-H., Wang P.-L., Rumble, III, D., Lippmann-Pipke J., Boice E., Pratt L. M., Sherwood Lollar B., Brodie E. L., Hazen T. C., Anderson G. L., DeSantis T. Z., Moser D. P., Kershaw D. and Onstott T. C. (2006) Long-term sustainability of a high-energy, low-diversity crustal biome. *Science* **314**, 479–482.
- Lippmann J., Stute M., Torgersen T., Moser D. P., Hall J. A., Lin L., Borcsik M., Bellamy R. E. S. and Onstott T. C. (2003) Dating ultra-deep mine waters with noble gases and ³⁶Cl, Witwatersrand Basin, South Africa. *Geochem. Cosmochim. Acta* **67**, 4597–4619.
- Lippmann-Pipke J., Sherwood Lollar B., Niedermann S., Stronck N. A., Naumann R., van Heerden E. and Onstott T. C. (2011) Neon identifies two billion year old fluid component in Kaapvaal Craton. *Chem. Geol.* **283**, 287–296.
- Liu Q. and Liu Y. (2016) Clumped-isotope signatures at equilibrium of CH₄, NH₃, H₂O, H₂S and SO₂. *Geochem. Cosmochim. Acta* **175**, 252–270.
- Lockridge J. P. (1977). Beecher Island Field Yuma County, Colorado. Rocky Mountain Association of Geologists 1977 Symposium: 271–279.
- Ma Q., Wu S. and Tang Y. (2008) Formation and abundance of doubly-substituted methane isotopologues (¹³CH₃D) in natural gas systems. *Geochem. Cosmochim. Acta* **72**(22), 5446–5456.
- Magnabosca C., Timmers P. H. A., Lau M. C. Y., Borgonie G., Linage-Alvarez B., Kuloyo O., Alleva R., Kieft T. L., Slater G. S., van Heerden E., Sherwood Lollar B. and Onstott T. C. (2016) The case for a dynamical subsurface ecosystem. *BioRxiv*. <http://dx.doi.org/10.1101/040204>.
- McCollom T. M. and Seewald J. S. (2006) Carbon isotope composition of organic compounds produced by abiotic synthesis under hydrothermal conditions. *Earth Planet. Sci. Lett.* **243**, 74–84.
- McCollom T. M. and Seewald J. S. (2007) Abiotic synthesis of organic compounds in deep-sea hydrothermal environments. *Chem. Rev.* **107**, 382–401.
- McKinney C. R., McCrea J. M., Epstein S., Allen H. A. and Urey H. C. (1950) Improvements in mass spectrometers for the measurement of small differences in isotope abundance ratios. *Rev. Sci. Instrum.* **21**(8), 724–730.
- Omar G. I., Onstott T. C. and Hoek J. (2003) The origin of deep subsurface microbial communities in the Witwatersrand Basin, South Africa as deduced from apatite fission track analyses. *Geofluids* **3**, 69–80.
- Ono S., Wang D. T., Gruen D. S., Sherwood Lollar B., Zahniser M. S., McManus B. J. and Nelson D. D. (2014) Measurement of a doubly substituted methane isotopologue, ¹³CH₃D, by tunable infrared laser direct absorption spectroscopy. *Anal. Chem.* **86**, 6487–6494.
- Onstott T. C., Moser D. P., Pffiffer S. M., Fredrickson J. K., Brockman F. J., Phelps T. J., White D. C., Peacock A., Balkwill D., Hoover R., Krumholz L. R., Broscik M., Kieft T. L. and Wilson R. (2003) Indigenous and contaminant microbes in ultradeep mines. *Environ. Microbiol.* **5**(11), 1168–1191.
- Proskurowski G., Lilley M. D., Kelley D. S. and Olson E. J. (2006) Low temperature volatile production at the Lost City Hydrothermal Field, evidence from a hydrogen stable isotope geothermometer. *Chem. Geol.* **229**, 331–343.

- Proskurowski G., Lilley M. D., Seewald J. S., Fruh-Green G. L., Olsen E. J., Lupton J. E., Sylva S. P. and Kelley D. S. (2008) Abiogenic hydrocarbon production at Lost City Hydrothermal Field. *Science* **319**, 604–607.
- Proskurowski G., Lilley M. D., Seewald J. S., Fruh-Green G. L., Olson E. J., Lupton J. E., Sylva S. P. and Kelley D. S. (2008) Abiogenic hydrocarbon production in Lost City hydrothermal field. *Science* **319**, 604–607.
- Qi Y., Yang J., Duan X., Zhu Y.-A., Chen D. and Holmen A. (2014) Discrimination of the mechanism of CH₄ formation in Fischer-Tropsch synthesis on Co catalysts: a combined approach of DFT, kinetic isotope effects and kinetic analysis. *Catal. Sci. Technol.* **4**, 3534–3542.
- Rockmann T., Popa M. E., Krol M. C. and Hofmann M. E. G. (2016) Statistical clumped isotope signatures. *Sci. Rep.* **6**. <http://dx.doi.org/10.1038/rsep31947>.
- Rowan E. (2006) Burial and Thermal History of the Central Appalachian Basin, Based on three 2-D Models of Ohio, Pennsylvania, and West Virginia. U. S. D. o. t. Interior. Geological Survey Open File Report 2006–1019.
- Scheller S., Goenrich M., Boecher R., Thauer R. K. and Juan B. (2010) The key nickel enzyme of methanogenesis catalyses the anaerobic oxidation of methane. *Nature* **465**, 606–609.
- Schoell M. (1988) Multiple origins of methane in the Earth. *Chem. Geol.* **71**, 1–10.
- Schrenk M. O., Brazelton W. J. and Lang S. Q. (2013). Serpentinization, Carbon, and Deep Life. Reviews in Mineralogy & Geochemistry, Carbon in Earth. (eds. R. M. Hazen, A. P. Jones and J. A. Baross). Chantilly, Mineralogical Society of America. **75**: 575-606
- Schilling R. D. (1964) Serpentinization as a possible cause of high heat-flow values in and near the oceanic ridges. *Nature* **201**, 807–808.
- Sessions A. L., Sylva S. P., Summons R. E. and Hayes J. M. (2004) Isotopic exchange of carbon-bound hydrogen over geologic timescales. *Geochem. Cosmochim. Acta* **68**(7), 1545–1559.
- Sherwood Lollar B., Westgate T. D., Ward J. A., Slater G. F. and Lacrampe-Couloume G. (2002) Abiogenic formation of gaseous alkanes in the Earth's crust as a minor source of global hydrocarbon reservoirs. *Nature* **416**, 522–524.
- Sherwood Lollar B., Lacrampe-Couloume G., Slater G. F., Ward J., Moser D. P., Gihring T. M., Lin L.-H. and Onstott T. C. (2006) Unravelling abiogenic and biogenic sources of methane in the Earth's deep subsurface. *Chem. Geol.* **226**, 328–339.
- Sherwood Lollar B., Voglesonger K., Lin L.-H., Lacrampe-Couloume G., Telling J., Abrajano T. A., Onstott T. C. and Pratt L. M. (2007) Hydrogeologic controls on episodic H₂ release from Precambrian fractured rocks – energy for deep subsurface life on Earth and Mars. *Astrobiology* **7**(6), 971–986.
- Sherwood Lollar B., Lacrampe-Couloume G., Voglesonger K., Onstott T. C., Pratt L. M. and Slater G. F. (2008) Isotopic signatures of CH₄ and higher hydrocarbon gases from Precambrian Shield sites: a model for abiogenic polymerization of hydrocarbons. *Geochem. Cosmochim. Acta* **72**, 4778–4795.
- Sherwood Lollar B., Onstott T. C., Lacrampe-Couloume G. and Ballentine C. J. (2014) The contribution of the Precambrian continental lithosphere to global H₂ production. *Nature* **14017**, 379–382.
- Simkus D. N., Slater G. F., Sherwood Lollar B., Wilkie K., Kieft T. L., Magnabosca C., Lau M. C. Y., Pullin M. J., Hendrickson S. B., Wommack K. E., Sakowski E. G., van Heerden E., Kuloyo O., Linage B., Borgonie G. and Onstott T. C. (2016) Variations in microbial carbon sources and cycling in the deep continental subsurface. *Geochem. Cosmochim. Acta* **173**, 264–283.
- Stolper D. A., Lawson M., Davis C. L., Ferreira A. A., Santos Neto E. V., Ellis G. S., Lewan M. D., Martini A. M., Tang Y., Schoell, Sessions A. L. and Eiler J. M. (2014a) Formation temperatures of thermogenic and biogenic methane. *Science* **344**, 1500–1503.
- Stolper D. A., Sessions A. L., Ferreira A. A., Santos Neto E. V., Schimmelmann A., Shusta S. S., Valentine D. L. and Eiler J. M. (2014b) Combined 13C-D and D-D clumping in methane: methods and preliminary results. *Geochem. Cosmochim. Acta* **126**, 169–191.
- Stolper D. A., Martini A. M., Clog M., Douglas P. M., Shusta S. S., Valentine D. L., Sessions A. L. and Eiler J. M. (2015) Distinguishing and understanding thermogenic and biogenic sources of methane using multiply substituted isotopologues. *Geochem. Cosmochim. Acta* **161**, 219–247.
- Takai K., Nakamura K., Toki T., Tsunogai U., Miyazaki M., Miyazaki J., Hirayama H., Nakagawa S., Nunoura T. and Horikoshi K. (2008) Cell proliferation at 122 °C and isotopically heavy CH₄ production by hyperthermophilic methanogen under high-pressure cultivation. *Proc. Natl. Acad. Sci.* **105**, 10949–10954.
- Tang Y., Perry J. K., Jenden P. D. and Schoell M. (2000) Mathematical modeling of stable carbon isotope ratios in natural gases. *Geochem. Cosmochim. Acta* **64**, 2673–2687.
- Tuttle O. F. (1949) Two pressure vessels for silicate-water studies. *Geol. Soc. Am. Bull.* **60**(10), 1727–1729.
- Valentine D. L. (2011) Emerging topics in marine methane biogeochemistry. *Ann. Rev. Mar. Sci.* **3**, 147–171.
- Wang W., Wang S., Ma X. and Gong J. (2011) Recent advances in catalytic hydrogenation of carbon dioxide. *Chem. Soc. Rev.* **40**, 3703–3727.
- Wang D. T., Gruen D. S., Sherwood Lollar B., Hinrichs K.-U., Stewart L. C., Holden J. F., Hristov A. N., Pohlman J. W., Morrill P. L., Könneke M., Delwiche K. B., Reeves E. P., Sutcliffe C. N., Ritter D. J., Seewald J. S., McIntosh J. C., Hemond H. F., Kubo M. D., Cardace D., Hoehler T. M. and Ono S. (2015) Nonequilibrium clumped isotope signals in microbial methane. *Science* **348**, 428–431.
- Ward J. A., Slater G. F., Moser D. P., Lin L.-H., Lacrampe-Couloume G., Bonn A. S., Davidson M., Hall J. A., Mislowski B., Bellamy R. E. S., Onstott T. C. and Sherwood Lollar B. (2004) Microbial hydrocarbon gases in the Witwatersrand Basin, South Africa: implications for the deep biosphere. *Geochem. Cosmochim. Acta* **68**, 3239–3250.
- Webb M. A. and Miller, III, T. F. (2014) Position-specific and clumped stable isotope studies: comparison of the Urey and path-integral approaches for carbon dioxide, methane, and propane. *J. Phys. Chem.* **118**, 467–474.
- Webster C. R., Mahaffy P. R., Atreya S. K., Flesch G. J., Mischna M. A., Meslin P., Farley K. A., Conrad P. G., Christensen L. E., Pavlov A. A., Martin-Torres J., Zorzano M.-P., McConnochie T. H., Owen T., Eigenbrode J. L., Glavin D. P., Steele A., Malespin C. A., Archer, Jr., P. D., Sutter B., Coll P., Freissinet C., McKay C. P., Moores J. E., Schwenzer S. P., Bridges J. C., Navarro-Gonzalez R., Gellert R., Lemmon M. T. and Team M. S. (2015) Mars methane detection and variability at Gale crater. *Science* **347**, 415–417.
- Whiticar M. J. and Etiope G. (2014) *Methane in Land-based Serpentinization Peridotites: New Discoveries and Isotope Surprises*. American Geophysical Union, San Francisco.
- Wongnate T., Sliwa D., Ginovska B., Smith D., Wolf M. W., Lehnert N., Rauei S. and Ragsdale W. (2016) The radical mechanism of biological methane synthesis by methyl-coenzyme M reductase. *Science* **352**(6288), 953–959.
- Yeung L. Y. (2016) Combinatorial effects on clumped isotopes and their significance in biogeochemistry. *Geochem. Cosmochim. Acta* **172**, 22–38.

- Young E. D., Rumble, III, D., Freedman P., Schauble E. and guo W. (2011) Inverted: high mass resolution gas-source mass spectrometry. *Mineral. Mag.* **73**, 2229.
- Young E. D., Rumble, III, D., Freedman P. and Mills M. (2016) A large-radius high-mass-resolution multiple-collector isotope ratio mass spectrometer for analysis of rare isotopologues of O₂, N₂, CH₄ and other gases. *Int. J. Mass Spectrom.* **401**, 1–10.
- Yoshinaga M. Y., Holler T., Goldhammer T., Wegener G., Phlman J. W., Brunner B., Kuypers M. M. M., Hinrichs K.-U. and Elvert M. (2014) Carbon isotope equilibration during sulphate-limited anaerobic oxidation of methane. *Nat. Geosci.* **7**, 190–195.
- Yu Y., Yang J., Hao C., Zhao X. and Wang Z. (2009) The adsorption, vibration and diffusion of hydrogen atoms on platinum low-index surfaces. *J. Comput. Theor. Nanosci.* **6**, 439–448.

Associate editor: Jochen J. Brocks